

This is an Open Access document downloaded from ORCA, Cardiff University's institutional repository: <https://orca.cardiff.ac.uk/id/eprint/135987/>

This is the author's version of a work that was submitted to / accepted for publication.

Citation for final published version:

Hasentab, E., Tusch, J., Schnabel, C., Marien, C. S., Van Kranendonk, M. J., Smithies, H., Howard, H., Maier, W. D. and Munker, C. 2021. Evolution of the early to late Archean mantle from Hf-Nd-Ce isotope systematics in basalts and komatiites from the Pilbara Craton. *Earth and Planetary Science Letters* 553 , 116627.
10.1016/j.epsl.2020.116627

Publishers page: <http://dx.doi.org/10.1016/j.epsl.2020.116627>

Please note:

Changes made as a result of publishing processes such as copy-editing, formatting and page numbers may not be reflected in this version. For the definitive version of this publication, please refer to the published source. You are advised to consult the publisher's version if you wish to cite this paper.

This version is being made available in accordance with publisher policies. See <http://orca.cf.ac.uk/policies.html> for usage policies. Copyright and moral rights for publications made available in ORCA are retained by the copyright holders.



1 Evolution of the early to late Archean mantle from Hf-Nd-Ce isotope 2 systematics in basalts and komatiites from the Pilbara Craton

3 E. HASENSTAB^{1*}, J. TUSCH¹, C.SCHNABEL^{1,2}, C. S. MARIEN¹, M. J. VAN KRANENDONK³, H. SMITHIES⁴, H.
4 HOWARD⁴, W. D. MAIER⁵, C. MÜNKER¹

5
6 ¹INSTITUT FÜR GEOLOGIE UND MINERALOGIE, UNIVERSITÄT ZU KÖLN, ZÜLPICHER STRASSE 49, 50674 COLOGNE,
7 GERMANY

8 ²ABTEILUNG NUKLEARCHEMIE, UNIVERSITÄT ZU KÖLN, ZÜLPICHER STRASSE 45, 50674 COLOGNE,
9 GERMANY

10 ³AUSTRALIAN CENTRE FOR ASTROBIOLOGY, UNIVERSITY OF NEW SOUTH WALES, KENSINGTON, NSW 2052,
11 AUSTRALIA

12 ⁴GEOLOGICAL SURVEY OF WESTERN AUSTRALIA, MINERAL HOUSE, 100 PLAIN STREET, EAST PERTH, WA 6004,
13 AUSTRALIA

14 ⁵SCHOOL OF EARTH AND OCEAN SCIENCES, CARDIFF UNIVERSITY, MAIN BUILDING, PARK PLACE, CARDIFF CF10
15 3AT, UNITED KINGDOM

16
17 *CORRESPONDING AUTHOR AT: UNIVERSITÄT ZU KÖLN, INSTITUT FÜR GEOLOGIE UND MINERALOGIE, ZÜLPICHER
18 STR. 49B, 50674 KÖLN, GERMANY.

19 TEL.: +49 221 470-89866

20 E-MAIL ADDRESS: chasens1@uni-koeln.de

21
22
23
24 Keywords: Archean; Hadean; Pilbara; komatiites; Hf-Nd; Ce-Nd; Lu-Hf; Sm-Nd; La-Ce; decoupling;
25 differentiation

26 Abstract

27 Inferences on the early evolution of the Earth's mantle can be deduced of long-lived radiogenic
28 isotope systems such as ¹⁷⁶Lu-¹⁷⁶Hf and ¹⁴⁷Sm-¹⁴³Nd, for which both parent and daughter elements
29 largely remain immobile at low metamorphic grades. However, it remains ambiguous when and to
30 what extent mantle-crust differentiation processes had started in the Archean. For a better
31 understanding of Archean mantle-crust evolution, we determined the initial ¹⁷⁶Lu-¹⁷⁶Hf, ¹⁴⁷Sm-¹⁴³Nd,
32 and, in a new approach, the ¹³⁸La-¹³⁸Ce isotope compositions of a suite of Archean mafic-ultramafic
33 rock samples from the 3.53-2.83 Ga old Pilbara Craton and 2.78-2.63 Ga old Fortescue Group in NW
34 Australia. These rocks represent one of the best-preserved Archean successions worldwide and
35 contain mafic-ultramafic rocks that were erupted during repeated and long-lived pulses of volcanism
36 throughout much of the Archean. Mantle-derived mafic-ultramafic rock samples were collected from
37 six major stratigraphic groups of the Pilbara Craton and the overlying Fortescue Group in order to
38 characterize the parental mantle source regions of the lavas and to reconstruct the temporal

39 evolution of the ambient mantle beneath this piece of cratonic lithosphere. In addition, we analyzed
40 contemporaneous TTG-like igneous suites and interbedded sediments in order to reconstruct the
41 lithospheric evolution of the Pilbara Craton.

42 The Hf-Nd-Ce isotope data imply the onset of mantle-crust differentiation in the Pilbara Craton as
43 early as ~ 4.2 Ga, well prior to any of the preserved stratigraphy. Within error, coupled Ce-Nd-Hf
44 isotope arrays all intersect chondritic values, implying that the Earth is of broadly chondritic
45 composition, also for the ^{138}La - ^{138}Ce isotope system. Mafic rocks usually yield strongly coupled $\epsilon\text{Hf}_{(i)}$,
46 $\epsilon\text{Nd}_{(i)}$ and $\epsilon\text{Ce}_{(i)}$ values that form a mixing line between an evolving depleted upper mantle
47 composition and the primitive mantle value ($\epsilon\text{Hf}_{(i)}$ ca. 0.0 to + 3.2, $\epsilon\text{Nd}_{(i)}$ ca. +0.2 to +1.7 and $\epsilon\text{Ce}_{(i)}$ ca.
48 +0.3 to -0.1). As all Paleoproterozoic samples lack co-variations between Nb/Th with $\epsilon\text{Hf}_{(i)}$ or $\epsilon\text{Nd}_{(i)}$,
49 contamination with an enriched crust is unlikely to explain this mixing trend. The most primitive
50 mafic samples show elevated Gd_N/Yb_N ratios (2.2-1.4), implying the involvement of a deep-rooted,
51 near-primitive, upwelling mantle that was progressively mixed into the depleted upper mantle. In
52 contrast to the mafic rocks, most, but not all komatiites are decoupled in their initial Hf-Nd-Ce
53 isotope compositions, by having extremely radiogenic $\epsilon\text{Hf}_{(i)}$ values at only moderately high $\epsilon\text{Nd}_{(i)}$ and
54 low $\epsilon\text{Ce}_{(i)}$ values. This decoupling is best explained by the assimilation of mantle domains that
55 underwent early melt depletion in the garnet stability field and evolved at high $^{176}\text{Lu}/^{176}\text{Hf}$ ratios but
56 at moderate $^{147}\text{Sm}/^{143}\text{Nd}$ and $^{138}\text{La}/^{138}\text{Ce}$ ratios over time. The disappearance of rocks with decoupled
57 Hf-Nd isotope compositions after ~ 3.2 Ga is likely linked to decreasing mantle temperatures that
58 were no longer able to melt such refractory mantle domains. Collectively, our new data for mafic
59 rocks from the Pilbara Craton confirms the presence of long-term depleted mantle domains in the
60 early Archean that are not sampled by the zircon Hf isotope record in the Pilbara Craton.

61

62 1. Introduction

63 The ^{176}Lu - ^{176}Hf and ^{147}Sm - ^{143}Nd decay systems have become key analytical tools for reconstructing
64 the early depletion history of the terrestrial mantle due to their robustness (e.g., Bennett et al., 1993;
65 Vervoort and Blichert-Toft, 1999; Hoffmann et al., 2011b). In contrast, the ^{138}La - ^{138}Ce system has only
66 rarely been applied to the early terrestrial rock record, because the slow radiogenic decay of ^{138}La to
67 ^{138}Ce ($\lambda=2.37\times 10^{-12} \text{ a}^{-1}$) and limited fractionation of La/Ce in igneous systems result in small Ce
68 isotope variations that are analytically difficult to resolve. During mantle-crust differentiation, Lu and
69 Sm are more compatible in the mantle compared to Nd and Hf, whereas La is more incompatible in
70 the mantle compared to Ce. Thus, depleted mantle domains will evolve towards positive initial $\epsilon\text{Hf}_{(i)}$
71 and $\epsilon\text{Nd}_{(i)}$, but towards negative $\epsilon\text{Ce}_{(i)}$ values. Hence, ^{138}La - ^{138}Ce systematics could, in principle, be
72 applied to similar geochemical issues as the ^{176}Lu - ^{177}Hf or ^{147}Sm - ^{144}Nd systems. As a consequence,
73 combined Ce-Nd-Hf isotope studies can place further constraints on early Earth differentiation
74 processes such as the observed decoupling of Hf-Nd isotopes in Archean rocks (e.g. Hoffmann et al.,
75 2011b; Rizo et al., 2011).

76 The Pilbara Craton is an excellent example to study the evolution of mantle-crust differentiation
77 processes on early Earth, due to long-lived volcanic pulses of mafic-ultramafic volcanism (Van
78 Kranendonk et al., 2002). For other cratons, such as the North Atlantic Craton, mantle evolution
79 processes have been complicated by secondary metamorphic events, which can disturb the Hf-Nd
80 isotope signatures of such highly metamorphosed rocks (e.g. Gruau et al., 1996; Hoffmann et al.,
81 2011b). In contrast, the majority of rocks from the Pilbara Craton have only been affected by low-
82 grade metamorphism, largely at lower greenschist facies and only locally at amphibolite facies
83 conditions (Collins and Van Kranendonk, 1999; Van Kranendonk et al., 2002). Although there exist
84 other cratons that contain older rocks, the well-preserved and low metamorphic grade
85 lithostratigraphic successions in the Pilbara Craton provide a near-continuous record of igneous
86 evolution for almost a billion years of Earth history, from 3.59-2.63 Ga (e.g., Van Kranendonk et al.,
87 2002; Smithies et al., 2007a; Petersson et al., 2019).

88 Based on predominantly positive $\epsilon\text{Nd}_{(t)}$ values, many studies on Pilbara mafic-ultramafic rock samples
89 suggest a moderately depleted mantle reservoir as a source for the dominantly mafic-ultramafic
90 greenstone belt stratigraphy (e.g., Gruau et al., 1987; Arndt et al., 2001; Smithies et al., 2007b).
91 However, previously reported Hf isotope data challenged these interpretations (Nebel et al., 2014;
92 Kemp et al., 2015; Petersson et al., 2019; Petersson et al., 2020). For example, studies on zircons by
93 Kemp et al. (2015) and Petersson et al., (2019, 2020) argued that the mantle beneath the Pilbara
94 Craton did not start to differentiate until ~ 3.6 Ga. In contrast Nebel et al. (2014) reported extremely
95 radiogenic $\epsilon\text{Hf}_{(t)}$ values in ~ 3.5 - 3.2 Ga komatiites, which requires a highly depleted mantle reservoir
96 to have been present already in the Hadean, a conclusion previously also reached by Tessalina et al.
97 (2010).

98 In this study, we present high-precision isotope dilution (ID) and isotope composition data for ^{176}Lu -
99 ^{176}Hf , ^{147}Sm - ^{143}Nd and ^{138}La - ^{138}Ce on a variety of rock samples from the Pilbara Craton in order to
100 better understand the long-term depletion history of the ambient mantle beneath the evolving
101 Pilbara Craton and the early Archean mantle in general. We analyzed 39 basalts and komatiites, five
102 granitoids, and three sedimentary rocks that were previously studied by Tusch et al. (2020) for their
103 major and trace element data, as well as for their ^{182}W isotope systematics. Furthermore, we
104 analyzed six basalts from the Jeerinah Formation that were provided by the Geological Survey of
105 Western Australia, as well as ten komatiites that were previously studied by Maier et al. (2009) for
106 platinum group element (PGE) concentrations. In total, we present combined ^{176}Lu - ^{176}Hf and ^{147}Sm -
107 ^{143}Nd systematics on 63 mantle-derived rocks, granitoids, and sediments. For a better understanding
108 of the ^{138}La - ^{138}Ce system in the Archean, we also report ^{138}La - ^{138}Ce data for a subset of 40 of these
109 samples. The data are evaluated with an emphasis on the temporal evolution of the Archean mantle
110 and source domain characteristics.

111

112 2. Geological setting

113 The Pilbara Craton is located in the northwestern part of Western Australia and is composed of
114 several distinct litho-tectonic terranes that contain thick successions of mafic-ultramafic and felsic
115 volcanic rocks (Van Kranendonk et al., 2007). The volcanic rocks erupted in several episodes lasting
116 from at least 3.59-2.63 Ga, accompanied by pulses of granitic magmatism over the range of 3.49-2.83
117 Ga. Typical dome-and-keel structures are preserved in the Paleoproterozoic nucleus of the East Pilbara
118 Terrane (EPT) (Fig. 1) (Van Kranendonk et al., 2004). The oldest unambiguous evidence for magmatic
119 activity in the Pilbara Craton is provided by 3.7-3.8 Ga inherited zircons (Van Kranendonk et al., 2002;
120 Kemp et al., 2015) and recently Petersson et al. (2019) have identified gabbroic enclaves (3.59-3.58
121 Ga Mount Webber Gabbro) that may be remnants of a mafic proto-crust.

122 Between ca. 3.53 and 3.23 Ga, cycles of mafic-ultramafic volcanism dominated the evolution of the
123 EPT, deposited in three unconformity-bound groups: the ca. 3.53-3.43 Ga Warrawoona Group, the
124 ca. 3.35-3.32 Ga Kelly Group and the 3.27-3.235 Ga Sulphur Springs Group (Van Kranendonk et al.,
125 2007; Hickman, 2012). From the increasingly thickened mafic crust, partial melts escaped and formed
126 repeated generations of felsic intrusions (Smithies et al., 2007a; Van Kranendonk, 2010; Wiemer et
127 al., 2018). The thickened mafic crust also acted as a thermal incubator, thus softening the middle
128 crust and causing gravitational instabilities (e.g., Collins and Van Kranendonk, 1999; Wiemer et al.,
129 2018). During gravitational collapse, the negatively buoyant overlaying mafic crust sank into the
130 middle crust, which, in turn, caused the rise of felsic domes and the typical dome-and-keel geometry
131 (Collins and Van Kranendonk, 1999; Van Kranendonk et al., 2004; Wiemer et al., 2018).

132 At ~3.2 Ga, plume-initiated rifting separated the Kurrana and Karratha terranes from the EPT, which
133 led to the eruption of the 3.18 Ga Soanesville Group and the contemporaneous Dalton Suite of
134 intrusive layered mafic-ultramafic rocks in the EPT (Van Kranendonk et al., 2007a, 2010). This rifting
135 event was recently interpreted in favor of the onset of Phanerozoic-style plate tectonics, and the
136 tectono-magmatic history of the craton between 2.9 and 3.2 Ga was interpreted to represent a full
137 Wilson cycle between 3.2-2.9 Ga (Van Kranendonk et al., 2010). This also includes the ~3.12 Ga
138 Whundo Group volcanics that provide evidence for subduction-related volcanism in the Pilbara
139 Craton (Smithies et al., 2007c). Between 3.07 to 2.91 Ga, the West Pilbara Superterrane (WPS), the

140 EPT, and the southeastern Kurrana Terrane accreted during three orogenic events (Van Kranendonk
141 et al., 2007), followed by deposition of the 3.02-2.92 Ga De Grey Supergroup in an extensional basin
142 (Van Kranendonk et al., 2007; Hickman, 2012) that was coeval with 2.935 Ga granitoid intrusions of
143 the Yule Granitic Complex. Volcanic rocks from the De Grey Supergroup show strongly enriched
144 geochemical characteristics indicating enriched, metasomatized mantle sources of possible
145 lithospheric mantle origin (Smithies et al., 2004).

146 Deposition of the 2.78-2.63 Ga Fortescue Group followed cratonization of the Pilbara Craton, which
147 was completed by the emplacement of ca. 2.83 granitoid rocks (Van Kranendonk et al., 2007). The
148 dominantly continental flood basaltic lavas of the Fortescue Group were fed by a series of large
149 feeder dykes, including the 2.78 Ga Black Range dolerite suite that erupted lavas of the lowermost
150 Mount Roe basalt (Arndt et al., 2001; Thorne and Trendall, 2001). The Fortescue Group lavas
151 originated from plume-generated komatiite volcanism that was contaminated by older crustal
152 basement, in a similar way to Phanerozoic large igneous provinces (Mole et al., 2018).

153

154 3. Methods

155 Analyses were performed on powder aliquots from 2-3 kg of rock sample grounded in an agate mill.
156 For Ce, Nd, and Hf measurements, 120-1200 mg of sample powder were digested in Parr® bombs.
157 For Sm/Nd and Lu/Hf measurements, mixed ^{149}Sm - ^{150}Nd and ^{176}Lu - ^{180}Hf isotope tracers were added
158 prior to digestion following previously described protocols (Münker et al., 2001; Hoffmann et al.,
159 2011a). For La-Ce (ID) measurements, a 20% aliquot was spiked with a ^{138}La - ^{142}Ce isotope tracer after
160 sample digestion. For isotope analysis we additionally added 1 ml of 65% HClO_4 to some replicates
161 after Parr® bomb digestions to prevent the formation of insoluble rare-earth elements (REE) and high
162 field strength (HFSE)-fluorides although addition of HClO_4 did not have an effect on the results of
163 concentration or isotope measurements (supplementary information S1). Lutetium-Hf separation
164 was performed following the analytical protocol of Münker et al. (2001). The light rare-earth element
165 (LREE)-bearing matrix from Lu-Hf separation as well as the 20% La-Ce ID aliquot were processed after

166 Schnabel et al. (2017). The leftover REE cut was then processed through Ln Spec resin after Pin and
167 Zalduegui (1997) to obtain pure Sm and Nd fractions. Total procedural blanks were always <150 pg
168 for Ce, <100 pg for La, <39 pg for Nd, <19 pg for Sm, and <140 pg for Hf and Lu, respectively, and
169 were all negligible.

170 All ID and isotope composition measurements were performed on a Thermo Fischer Neptune[®] or a
171 Thermo Fischer Neptune Plus[®] MC-ICP MS at Cologne. Lanthanum-Ce measurements were
172 performed following the protocol of Schnabel et al. (2017), but for Ce isotope composition
173 measurements, 10¹²Ω amplifiers were replaced by 10¹³Ω amplifiers. Mass bias correction was
174 performed by using the exponential law and a ¹³⁶Ce/¹⁴⁰Ce=0.002124072 (Makishima and Nakamura,
175 1991). All Ce data are reported relative to the Mainz-AMES standard solution (¹³⁸Ce/¹³⁶Ce=1.33738)
176 (Willbold, 2007). The tailing effect of ¹⁴⁰Ce on ¹³⁶Ce and ¹³⁸Ce was recorded by measuring the ratios of
177 half-masses relative to the peak mass (Willbold, 2007), but tail contributions on ¹³⁸Ce were always in
178 the sub-ppm range (e.g., Schnabel et al., 2017). For Ce ID measurements, Ba was used for mass bias
179 correction assuming a ¹³⁷Ba/¹³⁵Ba ratio of 1.70383, whereas for La ID measurements, Nd was used for
180 mass bias correction (¹⁴⁶Nd/¹⁴⁴Nd=0.7219). The external reproducibility for ¹³⁸Ce/¹³⁶Ce ratios is given
181 as relative standard deviation (RSD) and amounts to ±21 ppm (2 RSD), based on multiple
182 measurements (n=13) of six digestions of the reference material BHVO-2.

183 Neodymium isotope compositions are reported relative to a ¹⁴³Nd/¹⁴⁴Nd value of 0.511859 for La
184 Jolla standard. Mass bias correction followed the exponential law using a ¹⁴⁶Nd/¹⁴²Nd of 0.7219. The
185 external long-term reproducibility of Nd isotope measurements amounts to ±40 ppm (2 RSD) (cf.
186 Marien et al., 2019). Hafnium isotope compositions are given relative to the Münster AMES standard,
187 having a ¹⁷⁶Hf/¹⁷⁷Hf ratio of 0.282160 (Münker et al., 2001). All measured ¹⁷⁶Hf/¹⁷⁷Hf isotope data
188 were mass bias corrected by using the exponential law and a ¹⁷⁹Hf/¹⁷⁷Hf of 0.7325. Mass bias
189 correction for Lu measurements was performed by using a ¹⁷³Yb/¹⁷¹Yb ratio of 1.29197. The external
190 long-term reproducibility of ¹⁷⁶Hf/¹⁷⁷Hf analysis amounts to ±40 ppm (cf. Marien et al., 2019). The
191 external reproducibilities on ¹³⁸La/¹³⁶Ce ¹⁴⁷Sm/¹⁴⁴Nd and ¹⁷⁶Lu/¹⁷⁶Hf amount to ≤0.2% (2 RSD).

192 Calculated errors on our reported initial Hf-Nd-Ce isotope compositions represent the propagated
193 errors of the parent/daughter ratio, the age uncertainty and the external reproducibility given by
194 multiple digestions of reference materials.

195

196 4. Results

197 4.1. Major and trace element compositions

198 Major and trace element data for mafic-ultramafic samples of the ~3.53-3.31 Ga Warrawoona and
199 Kelly groups are broadly consistent with previously reported data for rocks from the EPT (Smithies et
200 al., 2007a; Smithies et al., 2018). For mafic-ultramafic samples, MgO contents generally vary between
201 4.11-29.2 wt.% (Fig. 2) (see Tusch et al. (2020) for further information on major and trace element
202 data). The concentrations of SiO₂ (43.7-54.1 wt.%), TiO₂ (0.218-2.00), and Al₂O₃ (4.88-14.9 wt.%) also
203 vary significantly (Fig. 2). Primitive mantle normalized trace element patterns of these samples are
204 predominantly flat, as indicated by moderate La/Yb_{CN} (0.546-3.32) and Gd/Yb_{PM} ratios (0.851-1.93)
205 (Fig. 3). Some mafic samples show minor depletions of Nb and Ta compared to La (Nb/La=0.568-1.14)
206 (Fig. 3). Ratios of Th/Yb are often lower (0.0535-0.697) when compared to previously published data
207 for EPT samples (Smithies et al., 2018). In most samples, Ce anomalies are absent (Ce/Ce*=0.917-
208 1.17), whereas Eu anomalies occur more frequently and range from 0.754-1.59.

209 The younger (c. 3.2 Ga) samples of the Soanesville Group, Dalton Suite, and Roebourne Group show
210 similar MgO (6.84-25.7 wt.%), Al₂O₃ (2.44-10.2 wt.%) and SiO₂ contents (40.0-51.4 wt.%) compared to
211 the older Warrawoona and Kelly Group samples, but exhibit significantly lower TiO₂ contents (0.170-
212 0.656 wt.%) (Fig. 2). Furthermore, these samples show depletions of LREE over heavy rare-earth
213 elements (HREE), as indicated by lower La/Yb_{CN} (0.761-4.27), and predominantly superchondritic
214 Sm/Nd ratios (0.229-0.372) as previously described (Smithies et al., 2007a, 2018). Compared to the
215 older Warrawoona and Kelly Group samples, Th/Yb (0.0834-0.229) are lower, Nb/La ratios define a

216 narrower range (0.464-0.738), and Eu and Ce anomalies are largely absent ($Ce/Ce^*=0.962-0.990$;
217 $Eu/Eu^*=0.963-1.27$).

218 Samples of the ~3.12-2.63 Ga Whundo Group, De Grey Supergroup, and the Fortescue Group show
219 generally the highest SiO_2 (48.8-56.7 wt.%) and Al_2O_3 (9.29-15.6 wt.%) contents and the lowest MgO
220 (5.29-15.6 wt.%), excluding two ultramafic rocks from the De Grey Supergroup ($MgO>30$ wt.%) (Fig.
221 2). Samples of the De Grey Supergroup have the highest incompatible trace element concentrations,
222 including substantial LREE enrichments relative to HREE ($La/Yb_{CN}=3.21-4.53$) (Fig. 3). Significant
223 depletions of Nb-Ta compared to La are present in most of these lithostratigraphic units
224 ($Nb/La=0.246-0.823$), although the most pronounced and uniform Nb-Ta anomalies are found in the
225 basalts and komatiites of the De Grey Supergroup ($Nb/La=0.246-0.339$). The oldest (~2.78 Ga)
226 Fortescue Group samples are also characterized by low Nb/La ratios (0.29-0.36) and incompatible
227 trace element patterns that are enriched in more incompatible trace elements ($La/Yb_{CN}=1.09-9.19$).
228 These samples stand in marked contrast to the youngest (~2.63 Ga) Fortescue Group samples
229 (Jeerinah Formation) that have predominantly flat primitive mantle normalized incompatible trace
230 element patterns ($La/Yb_{CN}=1.2-8.9$) (Fig. 3).

231

232 4.2. Radiogenic isotopes

233 A total of 63 samples were analyzed for their ^{176}Lu - ^{176}Hf and ^{147}Sm - ^{143}Nd isotope compositions and a
234 subset of 40 samples were analyzed for their ^{138}La - ^{138}Ce isotope compositions (supplementary
235 information S1). Age-corrected $\epsilon Hf_{(t)}$ and $\epsilon Nd_{(t)}$ values were normalized to the CHUR value of Bouvier
236 et al. (2008) and $\epsilon Ce_{(t)}$ values were normalized to the CHUR value of Willig and Stracke (2019) and
237 Israel et al., (2019), giving combined $^{138}La/^{136}Ce$ and $^{138}Ce/^{136}Ce$ ratios of 0.1865 and 1.336878,
238 respectively.

239 Initial $\epsilon Hf_{(t)}$ values of EPT basalts range from 0.0 to +4.2 (excluding sample Pil16-24 having an $\epsilon Hf_{(t)}$
240 value of +7.4), whereas komatiites tend to have higher $\epsilon Hf_{(t)}$ values (+1.5 to +8.1; see Supplementary

241 information S2), in accordance with previous observations by Nebel et al. (2014). Notably, negative
242 $\epsilon\text{Hf}_{(i)}$ and $\epsilon\text{Nd}_{(i)}$ values were only found in the youngest samples (De Grey Supergroup and Fortescue
243 Group; $\epsilon\text{Hf}_{(i)}=-2.7$ to $+5.0$; $\epsilon\text{Nd}_{(i)}=-2.8$ to $+3.2$). Felsic to intermediate granitic samples of various age
244 yield diverse $\epsilon\text{Hf}_{(i)}$ values (-5.8 to $+2.0$) and $\epsilon\text{Nd}_{(i)}$ values (-6.3 to $+1.3$) that are in good agreement
245 with previously reported zircon data (e.g., Kemp et al., 2015; Gardiner et al., 2017; Petersson et al.,
246 2019).

247 The majority of our samples display negative initial $\epsilon\text{Ce}_{(i)}$ values. Samples without Ce/Ce* anomalies
248 (Fig. 4) yield a narrow range in initial $\epsilon\text{Ce}_{(i)}$ values (-0.4 to $+0.61$), whereas samples with Ce/Ce*
249 anomalies show a significantly higher scatter in $\epsilon\text{Ce}_{(i)}$ values (-7.4 to $+2.3$). Generally, all three
250 isotope systems show the same trends between 3.53 Ga and 2.63 Ga, where $\epsilon\text{Hf}_{(i)}$ and $\epsilon\text{Nd}_{(i)}$ broadly
251 increase between 3.5-3.2 Ga, although the majority of 3.34 Ga basalt samples of the Kelly Group
252 deviate towards slightly more unradiogenic values (Fig. 5). Cerium isotopes show a complementary
253 trend, with decreasing $\epsilon\text{Ce}_{(i)}$ values between 3.5-3.2 Ga and a slight increase at 3.34 Ga. Between ca.
254 2.9-2.7 Ga, $\epsilon\text{Hf}_{(i)}$ and $\epsilon\text{Nd}_{(i)}$ decrease sharply, while $\epsilon\text{Ce}_{(i)}$ values increase slightly. The 2.63 Ga Jeerinah
255 Formation deviates from that trend by showing significantly higher $\epsilon\text{Hf}_{(i)}$ and $\epsilon\text{Nd}_{(i)}$, as well as lower
256 $\epsilon\text{Ce}_{(i)}$ values.

257

258 5. Discussion

259 5.1. Alteration and its effects on radiogenic isotope systematics

260 Rocks from the Pilbara Craton have experienced a complex geological history, including hydrothermal
261 alteration and metamorphism that subsequently modified the pristine geochemistry of these rocks
262 (Collins and Van Kranendonk, 1999; Van Kranendonk et al., 2002). Thus, it is crucial to evaluate
263 whether the samples analyzed in this study have preserved their primary REE and HFSE budgets.
264 HFSE, Th, and REE display significant co-variations with Zr, indicating that these elements have not
265 been substantially mobilized by secondary processes (Fig. 2) (see also Polat et al., 2002). Cerium

266 anomalies in mafic samples are always smaller than 5% (excluding sample Pil16-44a: Ce/Ce*=1.2 and
267 sample 179757: Ce/Ce*=0.92), indicating that the LREE were not substantially mobilized during
268 secondary geological events (Fig. 4a) (Polat et al., 2002). Similar to previous studies on Archean rocks
269 (e.g. Vervoort and Blichert-Toft, 1999; Nebel et al., 2014), initial $\epsilon\text{Hf}_{(i)}$ and $\epsilon\text{Nd}_{(i)}$ values (and also $\epsilon\text{Ce}_{(i)}$
270 values) show a coherent evolution through time (Fig. 5). Furthermore, there are no co-variations
271 between $\epsilon\text{Hf}_{(i)}$, $\epsilon\text{Nd}_{(i)}$, and $\epsilon\text{Ce}_{(i)}$ and loss on ignition (LOI) and all three parent/daughter ratios
272 correlate with each other, indicating primary magmatic trends (Figs. 4b and 4c). In contrast, all large
273 ion lithophile elements were mobile during post-magmatic events, as suggested by poor correlations
274 with Zr (Fig. 2f).

275 In marked contrast to the mafic rocks, most granitoids display negative Ce/Ce* anomalies, as low as
276 0.835, that increase with increasing SiO₂ (Fig. 4a). This is surprising, as the granitoids studied have
277 preserved a seemingly pristine mineralogy and have very low LOIs (<1.5 wt %). The Ce/Ce* anomalies
278 imply that the granitoids are prone to disturbance of the ¹³⁸La-¹³⁸Ce system, likely during oxidative
279 weathering, where Ce⁴⁺ can become decoupled from the other REE³⁺. We speculate that altered
280 mafic volcanic rocks are less susceptible to terrestrial weathering than granites, as the mafic
281 volcanics contain high amounts of secondary minerals (e.g., chlorite serpentine, epidote and
282 amphibole) that might be more robust during oxidative terrestrial weathering.

283 The coupled behavior of $\epsilon\text{Hf}_{(i)}$, $\epsilon\text{Nd}_{(i)}$, and $\epsilon\text{Ce}_{(i)}$ in mafic-ultramafic Pilbara rocks (Fig. 5) also argues
284 against secondary alteration effects, as the three studied radioactive decay systematics should be
285 variably affected by secondary alteration (e.g., Polat et al., 2002). Most importantly, all whole rock
286 ¹⁴⁷Sm-¹⁴³Nd and ¹⁷⁶Lu-¹⁷⁶Hf (and ¹³⁸La-¹³⁸Ce) age regression lines for individual units yield ages which
287 overlap within error with the reported stratigraphic ages for the formations from which they were
288 sampled (Supplementary Figs. 1-3). Thus, we conclude that the initial Hf-Nd-Ce isotope compositions
289 determined in this study are sufficiently robust to constrain the depletion history of the Archean
290 mantle beneath the Pilbara Craton, although ¹³⁸La-¹³⁸Ce data for samples with Ce/Ce* anomalies are
291 regarded as altered.

292

293 5.2. Effects of crustal contamination

294 Crustal contamination can strongly affect radiogenic isotope compositions and consequently obscure
295 the information on parental mantle sources. The oldest mafic-ultramafic samples in our study (3.53-
296 3.18 Ga) show a broad range of $\epsilon\text{Hf}_{(i)}$ and $\epsilon\text{Nd}_{(i)}$, correlating with La/Yb (Fig. 6f) but not with Nb/Th
297 (Fig. 6d). This implies that the magmatic source mixed with a second isotopically heterogeneous
298 component, but this was unlikely continental crust as it has characteristically low Nb/Th ratios.
299 Similar co-variations are also expected for Ce isotopes, but such changes are not easily analytically
300 resolvable. As most of the 3.53-3.18 Ga mafic samples also fall on the MORB-OIB array in Th/Yb vs.
301 Nb/Yb space (Fig. 6a), it seems more plausible that the two components involved were primitive
302 mantle-like source and a more depleted mantle endmember.

303 Unlike the older mafic samples, younger units (De Grey Supergroup, Fortescue Group, and potentially
304 the Whundo Group) show decreasing Nb/Th with decreasing $\epsilon\text{Hf}_{(i)}$ (Fig. 6c). This observation is best
305 explained by the interaction of primary melts with an enriched component, likely continental
306 crust (Arndt et al., 2001; Mole et al., 2018), but possibly also mantle source enrichment (Smithies et
307 al., 2005a).

308

309

310 5.3. Cerium isotope constraints

311 Although the ^{138}La - ^{138}Ce system has so far only rarely been applied in geochemistry, it can put
312 additional constraints on the implications that are drawn from combined ^{176}Lu - ^{176}Hf and ^{147}Sm - ^{143}Nd
313 systematics, e.g. the origin of strongly decoupled Hf and Nd isotope compositions found in Archean
314 mafic rock successions (Vervoort and Blichert-Toft, 1999; Vervoort et al., 2000; Hoffmann et al.,
315 2011b). One process that was inferred for this decoupling is the fractionation of Ca-perovskite during
316 magma ocean crystallization (e.g. Hoffmann et al., 2011b; Rizo et al., 2011). In the presence of
317 perovskite, LREE can be strongly fractionated from Lu and Hf (Corgne and Wood, 2002; Corgne et al.,
318 2005). In the lower mantle, the LREE are mainly affected by the fractionation of Ca- and Mg-
319 perovskite that have $D_{\text{La}} < D_{\text{Ce}}$ and $D_{\text{Sm}} > D_{\text{Nd}}$, causing perovskite cumulates to have superchondritic
320 Sm/Nd ratios but subchondritic La/Ce ratios (Fig. 4c). Although Ca-perovskite is less abundant than
321 Mg-perovskite, all the LREE are significantly more compatible in the former ($D_{\text{LREE}} > 1$) than the latter
322 phase ($D_{\text{LREE}} < 1$). Lutetium and Hf show the opposite behavior during perovskite fractionation with
323 $D_{\text{Lu}}/D_{\text{Hf}} \sim 0.5$ for Mg-perovskite, and $D_{\text{Lu}}/D_{\text{Hf}}$ ratio of > 5 for Ca-perovskite (Corgne and Wood, 2002;
324 Corgne et al., 2005). Consequently, early segregation of Ca- and Mg-perovskite would produce
325 perovskite cumulates that exhibit lower La/Ce and higher Sm/Nd ratios compared to bulk silicate
326 Earth, whereas the Lu/Hf ratio is variable, and strongly dependent on the fractions of Ca- and Mg-
327 perovskite being crystallized (e.g. Hoffmann et al., 2011b; Rizo et al., 2011; Puchtel et al., 2016).
328 Thus, early Ca-Mg-perovskite cumulates would evolve towards negative ϵ_{Ce} values, positive ϵ_{Nd}
329 values, and variable ϵ_{Hf} values.

330 To further quantify this process, we conducted trace element modeling, assuming crystallization of
331 4.5% Ca-perovskite, 85% Mg-perovskite, and 10.5% ferropericlasite, in accord with previous estimates
332 (e.g. Hoffmann et al., 2011b; Puchtel et al., 2016; Rizo et al., 2016) (see Supplementary information
333 S2). Higher abundances of Ca-perovskite would generate extremely unradiogenic Hf isotope
334 compositions over time, whereas lower Ca-perovskite abundances would result in extremely positive

335 Zr-Hf anomalies relative to REE. The age for the magma ocean crystallization was set to 4.4 Ga,
336 although changing that age by ± 100 Ma hardly affects the isotopic outcome at 3.5 Ga. Depending on
337 the style of crystallization (fractional vs. equilibrium crystallization) and the fraction of crystallized
338 melt (5% to 60%), perovskite cumulates in both crystallization modes develop towards positive ϵ_{Nd}
339 values (ca. +0.8 to +5.5), variable ϵ_{Hf} values (-5.4 to +3.0), and strongly negative ϵ_{Ce} values (-1.0 to -
340 1.5) at 3.5 Ga. The ϵ_{Ce} values of these modelled cumulates at 3.5 Ga would be significantly lower
341 than ϵ_{Ce} values of our oldest 3.53-3.34 Ga samples from the EPT (-0.3 to +0.3) (Fig. 5c). The exotic
342 isotope composition that is derived from our model is unmatched by our observed data and thus
343 precludes Ca-Mg perovskite cumulates to be a potential source for Pilbara rocks, which is
344 furthermore consistent with relatively high $^{138}\text{La}/^{136}\text{Ce}$ ratios in our samples (Fig. 4c) and an
345 insignificant fractionation of Zr-Hf from Sm-Nd (Fig. 3). Altogether, the geochemical evidence
346 suggests that the decoupling of Hf-Nd isotopes in the Pilbara Craton does not stem from an early
347 magma ocean crystallization event, but rather originates from early differentiation events in the
348 upper mantle.

349 The combination of Ce, Nd and Hf isotopes provide a powerful tool to gain better insight into the
350 history of the early Earth and demonstrate that Ca-Mg cumulate segregation during magma ocean
351 crystallization can be discarded as a cause for extremely high $\epsilon_{\text{Hf}(t)}$ values found in Archean rocks
352 from the Pilbara Craton. It still remains ambiguous, however, if the decoupling of Hf and Nd isotopes
353 in other Archean rocks can be explained by perovskite segregation (e.g., Hoffmann et al., 2011b;
354 Puchtel et al., 2016; Rizo et al., 2016) or not (e.g., Hoffmann and Wilson, 2017), although future ^{138}La -
355 ^{136}Ce isotope studies might help to place better constraints on this issue.

356

357 5.4. Hafnium, Nd and Ce isotope systematics of Pilbara mafic-ultramafic rocks and their
358 implications for mantle evolution

359 Some mafic-ultramafic rocks from the Pilbara Craton show a decoupling of their initial Hf-Nd-Ce
360 isotope compositions, with extremely radiogenic $\epsilon\text{Hf}_{(t)}$ values up to +8.1 at significantly lower $\epsilon\text{Nd}_{(t)}$
361 values (Figs. 5a and 7b). These findings are in apparent contrast to the studies by Kemp et al. (2015)
362 and Petersson et al., (2019; 2020) who postulated a near-chondritic mantle at ~ 3.6 Ga. Their studies
363 focused on Hf isotope compositions measured in inherited and detrital zircons from granitoids and
364 sedimentary rocks (Kemp et al., 2015) and zircons from mafic to felsic rock successions (Petersson et
365 al., 2019; Petersson et al., 2020). However, zircons in granitoids may not reveal the full depletion
366 history of the Archean mantle, and in particular the TTGs that are thought to result from remelting of
367 older mafic protoliths (Smithies et al., 2009; Hoffmann et al., 2011a; Gardiner et al., 2017; Johnson et
368 al., 2017). Depending on the time elapsed between mantle melting, formation of mafic proto-crust,
369 and TTG formation (hereafter the crustal residence time), the mafic protolith may have developed
370 unradiogenic Hf isotope compositions. Consequently, zircons that grew during TTG crystallization
371 may have inherited their initial Hf isotope compositions from the evolved isotope composition of the
372 mafic protolith rather than from the ambient mantle.

373 Petersson et al., (2019; 2020) reported chondrite-like Hf isotope compositions for 3.59-3.31 Ga
374 zircons from mafic to intermediate rocks from the Pilbara Craton, from which they argued for a
375 chondritic composition of the ambient mantle until ~ 3.6 Ga. However, the basalts of their study show
376 significant LREE enrichment and strong Nb-Ta depletions. Based on our study, this is best explained
377 by the interaction with an enriched component, most likely reflecting crustal contamination. This is
378 also in accord with previous work by Smithies et al., (2018) who have found evidence for crustally
379 contaminated ~ 3.5 Ga Pilbara basalts displaying similarly low Nb/Th ratios as those reported by
380 Petersson et al., (2019). Moreover, the presence of basalts with near-chondritic $\epsilon\text{Hf}_{(t)}$ does not
381 exclude the presence of more depleted mantle, as shown by our study (Figs. 5-8). If such rocks are
382 interpreted as crustally contaminated, as we favor, they rather provide evidence for the presence of
383 ≥ 3.59 Ga felsic basement beneath the Pilbara Craton, which is consistent with inherited zircon data
384 (Van Kranendonk et al., 2002).

385 Due to the predominantly positive $\epsilon\text{Hf}_{(i)}$ and $\epsilon\text{Nd}_{(i)}$ values in mafic-ultramafic rocks analyzed here, we
386 conclude that the ambient mantle of the Pilbara Craton must have undergone older depletion events
387 prior to 3.5 Ga, as suggested by previously studies (Gruau et al., 1987; Arndt et al., 2001; Smithies et
388 al., 2007b; Tesselina et al., 2010; Nebel et al., 2014; Gardiner et al., 2017). Hafnium and Nd isotope
389 compositions both suggest an onset of mantle-crust differentiation processes at ~ 4.2 Ga, evolving
390 towards present day ϵHf and ϵNd values of +16 and +10, respectively. In contrast, Ce isotopes are not
391 able to place further constraints on that depletion event due to somewhat smaller isotope
392 variations, although Ce isotope evidence is still in accord with a ~ 4.2 Ga depletion event (assuming a
393 present day ϵCe of the depleted upper mantle of -1.5). Nevertheless, there are some samples with
394 near-chondritic $\epsilon\text{Hf}_{(i)}$ and $\epsilon\text{Nd}_{(i)}$ values that lack evidence for crustal contamination (Pil16-17, Pil16-
395 20b). These samples likely originated from more primitive mantle sources, possibly from primitive
396 upwelling mantle material added to the depleted upper mantle (cf. Bédard, 2018). Importantly,
397 however, we observe an increase in $\epsilon\text{Hf}_{(i)}$ and $\epsilon\text{Nd}_{(i)}$ and a decrease in $\epsilon\text{Ce}_{(i)}$ with decreasing
398 crystallization age between 3.53 Ga and 3.12 Ga. This is best explained by a depleted mantle source
399 that evolved through geologic time (cf. Smithies et al., 2005b).

400 Initial Hf and Nd isotope compositions in rocks from the slightly younger (~ 3.26 -3.18 Ga) Roebourne
401 Group, Soanesville Group and Dalton Suite that are all ascribed to a rift-related setting are
402 significantly more radiogenic, with $\epsilon\text{Ce}_{(i)}$ being more unradiogenic, if compared to samples of the
403 3.34 Ga old Kelly Group (Arndt et al., 2001; Smithies et al., 2007b; Van Kranendonk et al., 2010). In
404 addition, the majority of samples from these younger successions are characterized by elevated
405 Sm/Nd ratios and MORB-like trace element patterns, implying a more depleted mantle source
406 compared to the plume-related rocks of the Warrawoona and Kelly groups, as previously postulated
407 by Smithies et al. (2005b). The observed change in the trace element geochemistry is likely linked to
408 a proposed change in geodynamic setting at ~ 3.2 Ga from upwelling/plume-like dominated processes
409 to modern style plate tectonics (Smithies et al., 2005a; Smithies et al., 2005b; Van Kranendonk et al.,
410 2007; Van Kranendonk et al., 2010). We conclude that this change from mantle upwelling/plume-

411 related volcanism before ~3.2 Ga to rift-related volcanism after ~3.2 Ga (Smithies et al., 2005b; Van
412 Kranendonk et al., 2010) is mirrored by a change in ambient mantle composition. Such a model is
413 also in accord with observations of increasing PGE abundances (Maier et al., 2009) and decreasing
414 ^{182}W isotope anomalies (Tusch et al., 2020) at the same time, which are suggested to mirror
415 widespread homogenization of the mantle at this time by more efficient vertical mixing. The long-
416 lived isotope systems analyzed in this study can help to better constrain how the involvement of
417 different mantle reservoirs triggered homogenization of late veneer material. Between 3.5 and 3.2
418 Ga, deep-rooted upwelling mantle material that was not yet equilibrated with late veneer material
419 mixed with shallower mantle regions that already equilibrated with late veneer material. Due to a
420 change in the geodynamic setting at 3.2 Ga (Van Kranendonk et al., 2010), the supply in the upper
421 mantle by upwelling mantle with pre-late veneer signature ceased, resulting in decreased $\mu^{182}\text{W}$
422 values (Tusch et al., 2020) and increased PGE concentrations (Maier et al., 2009) after ~3.2 Ga.

423 With the emergence of localized subduction by ~3.1 Ga, an arc-like setting led to formation of the
424 3.12 Ga Whundo Group (Krapez and Eisenlohr, 1998; Smithies et al., 2005a; Smithies et al., 2007c) .
425 Our data for Whundo Group samples generally indicate the involvement of an enriched component
426 as implied by somewhat lower Nb/Th ratios and $\epsilon\text{Hf}_{(t)}$ and $\epsilon\text{Nd}_{(t)}$ values in these samples (Figs. 3, 5,
427 6c). In the context of a subduction-like setting that was previously proposed for the Whundo Group
428 (Krapez and Eisenlohr, 1998; Smithies et al., 2005a; Smithies et al., 2007c), it is possible that this
429 enriched component originates from remelting a subducting crust. However, the small number of
430 samples (n=3) analyzed from the Whundo Group hampers a more detailed interpretation of the
431 tectonic setting of the Whundo Group. After the collision of the WPS and the EPT at 3.07 Ga,
432 volcanics of the ~3.0 Ga De Grey Supergroup tapped a metasomatized mantle that was likely re-
433 enriched within a subduction setting at ~3.12 Ga (Smithies et al., 2004; Smithies et al., 2005a). This is
434 mirrored by significantly lower $\epsilon\text{Hf}_{(t)}$ and $\epsilon\text{Nd}_{(t)}$ and higher $\epsilon\text{Ce}_{(t)}$ values in all of the rocks of the De
435 Grey Supergroup (Fig. 5). The absence of samples that have positive $\epsilon\text{Hf}_{(t)}$, $\epsilon\text{Nd}_{(t)}$ and lower $\epsilon\text{Ce}_{(t)}$

436 values argues against a role of AFC processes and supports evidence that the enriched component
437 must have already been distributed within the mantle source (Smithies et al., 2004).

438 The older units (2.78-2.63 Ga) of the Fortescue Group were contaminated by significantly older crust,
439 as indicated by AFC processes becoming apparent from strongly negative $\epsilon\text{Hf}_{(i)}$ and $\epsilon\text{Nd}_{(i)}$ and positive
440 $\epsilon\text{Ce}_{(i)}$ values that are found in some samples of the Fortescue Group (Arndt et al., 2001; Smithies et
441 al., 2007b; Mole et al., 2018). In contrast, the majority of the younger ~ 2.63 Ga Jeerinah Formation
442 within the Fortescue Group show no evidence for crustal contamination (except possibly sample
443 201476), by generally having elevated $\epsilon\text{Hf}_{(i)}$ (+4.2 to +5.0) and $\epsilon\text{Nd}_{(i)}$ (+0.5 to +3.2), and low $\epsilon\text{Ce}_{(i)}$
444 values (-0.44 to -1.3), suggesting an origin from a depleted mantle domain.

445

446 5.5.A genetic model for the evolution of the East Pilbara Terrane

447 Our Hf and Nd isotope results reveal distinct differences between most komatiites and basalts. As
448 $\epsilon\text{Hf}_{(i)}$ values are significantly higher in komatiites compared to most basalts, different mantle
449 reservoirs must have been involved in the formation of the Pilbara Craton. Furthermore, the majority
450 of basalts from the Warrawoona Group have $\epsilon\text{Hf}_{(i)}$ and $\epsilon\text{Nd}_{(i)}$ values that are best explained by an
451 origin from a shallow, depleted upper mantle domain (Gruau et al., 1987; Nisbet et al., 1993; Arndt
452 et al., 2001; Smithies et al., 2005b; Smithies et al., 2007b; Sossi et al., 2016; Bédard, 2018).
453 Nevertheless, some samples investigated here show near-chondritic $\epsilon\text{Hf}_{(i)}$, $\epsilon\text{Nd}_{(i)}$ and $\epsilon\text{Ce}_{(i)}$ values that
454 cannot be explained by crustal contamination. This observation rather implies near-primitive mantle
455 sources for at least some rocks from the Pilbara Craton that likely represent material from deep-
456 rooted upwelling mantle (see also Van Kranendonk et al., 2007a, 2015). However, it is still ambiguous
457 whether komatiites in general were formed in a plume setting (e.g., Arndt et al., 1997; Arndt et al.,
458 2001; Smithies et al., 2005b) or as a consequence of mantle overturn events (e.g., Bédard, 2018). As
459 our model can be applied to both scenarios, we refer to this process as '*upwelling mantle*' without
460 preferring any of these two processes.

461 Interestingly, two Warrawoona Group samples (Pil16-17 and Pil16-20b) of this study that display
462 chondritic Hf-Nd-Ce isotope compositions were melted in deeper parts of the mantle, as indicated by
463 the highest $Gd/Yb_{PM}=1.72-1.93$ and $TiO_2/Yb=0.752-0.738$. Pressure and temperature estimates
464 following the approach of Lee et al. (2009) confirm that sample Pil16-20b was melted at P-T
465 conditions exceeding the estimates for all other Warrawoona Group samples from the Pilbara Craton
466 by at least 3 GPa and 150°C (Supplementary Fig. 4; sample Pil16-17 could not be calculated). In
467 contrast, all other Warrawoona Group samples with more radiogenic $\epsilon Hf_{(t)}$ and $\epsilon Nd_{(t)}$ values were
468 melted in shallower mantle regions as indicated by near-chondritic Gd/Yb_{PM} . As the Paleoproterozoic
469 basalts from this study show a continuous spectrum from near-chondritic to increasingly positive
470 $\epsilon Hf_{(t)}$ and $\epsilon Nd_{(t)}$ values expected for depleted mantle at that time, we conclude that a upper depleted
471 mantle endmember was mixed with a near-chondritic upwelling mantle between 3.53-3.34 Ga (Figs.
472 5-8).

473 In contrast to the majority of the basalts analyzed here, most komatiitic rocks and one basalt from
474 the EPT show highly radiogenic initial Hf isotope compositions that are decoupled from their Nd-Ce
475 isotope compositions. This decoupling can be explained by older melt loss from garnet-bearing
476 residual mantle reservoirs that can efficiently fractionate Lu/Hf from Sm/Nd and La/Ce.

477 In order to reconcile our observations, we conducted isotope and trace element modelling to explain
478 the decoupled Hf-Nd-Ce isotope compositions, as well as the trace element characteristics of rocks
479 from the Pilbara Craton. Following Sossi et al. (2016), a non-modal batch melting model was used.
480 The first step comprised extraction of 10% melt from a lherzolite in the garnet stability field at 4.2 Ga,
481 forming residual mantle domains. We have chosen this age based on our data, as it likely reflects the
482 onset of mantle-crust differentiation beneath the Pilbara Craton (Fig. 5). Within 700 Ma, such
483 isolated residual mantle domains may have evolved towards extreme $\epsilon Hf_{(t)}$, $\epsilon Nd_{(t)}$ and $\epsilon Ce_{(t)}$ values of
484 +42, +16 and -1.2, respectively, in accord with present day observations from abyssal peridotites
485 (Salters et al., 2011). Due to the refractory nature of such depleted mantle domains, higher melting
486 temperatures are required, which can explain why the decoupling of Hf-Nd-Ce isotope compositions

487 is mainly found in komatiites as they are a product of high temperature mantle melting (e.g., Arndt et
488 al., 1997). This model can also explain the highly radiogenic but coupled Hf and Nd isotope
489 compositions of sample 179757, where the residual mantle contains more clinopyroxene than
490 orthopyroxene (see Supplementary information S3). Mass balance calculations, as illustrated in
491 Supplementary Figure 5, suggest that in-mixing of more fertile primitive mantle material would
492 efficiently dilute the Hf-Nd-Ce isotope compositions of such residual domains. Our model
493 demonstrates that mixing between primitive mantle with Hadean residual mantle at almost equal
494 proportions (30-50% residual mantle and 50-70% primitive mantle) creates a hybrid mantle source
495 with trace element and Hf-Nd-Ce isotope characteristics that match those observed in rocks from the
496 Pilbara Craton (Fig. 7, Supplementary Fig. 5).

497 Unfractionated $Gd/Yb_{PM}=0.851-1.25$ and relatively low TiO_2/Yb ratios of all EPT komatiites suggest
498 melting within the spinel stability field, in accord with P-T estimates for the Warrawoona Group (Lee
499 et al., 2009) (Supplementary Fig. 4). This apparent contrast to our proposed residual mantle domains
500 from the garnet stability field can be explained by two processes: (1) Anomalously high temperatures
501 of the upwelling mantle shifted the spinel stability field towards significantly higher depths (e.g.,
502 Klemme et al., 2009); or (2) convective transport of the residual mantle domains to shallower depths
503 outside the garnet stability field, as previously proposed for the 3.33 Ga Comondale komatiite suite
504 in South Africa (Hoffmann and Wilson, 2017 and refs. therein). As previously observed by Nebel et al.
505 (2014), and confirmed here, the extremely radiogenic $\epsilon Hf_{(t)}$ values in Pilbara komatiites are absent
506 after ~ 3.2 Ga (Fig. 5), consistent with the proposed change in plate tectonic regime recorded in the
507 Pilbara Craton. As the onset of Phanerozoic-style plate tectonics has long been interpreted to result
508 from decreasing mantle temperatures (cf. Davies, 1992), we therefore conclude that it was this
509 factor, more than any other, that reduced the proportions of residual mantle domains tapped by
510 mantle melts after 3.2 Ga.

511

512 6. Conclusions

513 A combined Hf-Nd-Ce isotope dataset for mafic-ultramafic rocks from the Pilbara Craton, covering all
514 major stratigraphic units, places new constraints on the geodynamic evolution of the Pilbara Craton
515 and the early Archean mantle in general. In mafic-ultramafic successions of the Pilbara Craton, these
516 isotope systematics were insignificantly affected by post-magmatic alteration, implying that the
517 decoupling of Hf isotopes from Nd-Ce isotopes is a primary magmatic feature. Consistently elevated
518 Nb/La ratios in all samples >3.2 Ga preclude AFC processes to have operated during their formation,
519 possibly reflecting the limited extent of evolved continental crust in the Pilbara Craton during the
520 early Archean.

521 Perovskite fractionation in an ancient magma ocean cannot explain the observed variability in Hf-Nd-
522 Ce isotope compositions, and the Ce-Nd array of the accessible upper mantle was near-chondritic by
523 early Archean time. Rather, the broad variety of $\epsilon\text{Hf}_{(t)}$, $\epsilon\text{Nd}_{(t)}$ and $\epsilon\text{Ce}_{(t)}$ values imply that at least two
524 distinct mantle reservoirs were involved in the formation of these rocks. One reservoir, most likely
525 ambient upper mantle, must have had a long depletion history, commencing at ~ 4.2 Ga, as
526 constrained by the most depleted basalt samples. A second reservoir with near-chondritic radiogenic
527 isotope ratios likely tapped the lower mantle by continuous mantle upwelling. Most komatiites have
528 significantly higher $\epsilon\text{Hf}_{(t)}$ values that are decoupled from Nd-Ce compositions. This is likely explained
529 by high temperature melting of residual mantle domains that have experienced a previous melt
530 depletion history in the garnet stability field.

531 Samples younger than 3.2 Ga exhibit significantly lower Nb/La ratios and, in some cases,
532 unradiogenic Hf and Nd isotope compositions, reflecting the involvement of enriched components
533 via subduction zone recycling and crustal contamination. Collectively, our study demonstrates that
534 the radiogenic isotope composition of mafic-ultramafic rocks from Pilbara Craton provides an
535 unprecedented insight into mantle depletion history, further illustrating that depletion of the mantle
536 may have commenced relatively early in Earth's history, in late Hadean time.

537

538

539 Acknowledgements

540

541 E.H and C.M. acknowledge funding through the European Commission by ERC grant 669666 'Infant
542 Earth'. F. Wombacher, and A. Katzemich and other laboratory support staff are thanked for their
543 support in the Lab. S. Kommescher is thanked for helpful discussions. H. Smithies and H. Howard
544 publish with the permission of the Executive Director of the Geological Survey of Western Australia.
545 We thank Nicholas Gardiner and Oliver Nebel for constructive reviews that helped to improve the
546 manuscript and we also thank Frederic Moynier for editorial handling.

547

548 References

- 549 Arndt N., Bruzak G. and Reischmann T. (2001) The oldest continental and oceanic plateaus:
550 geochemistry of basalts and komatiites of the Pilbara Craton, Australia. In: *Ernst, R.E., Buchan,*
551 *K.L. (Eds.), Mantle Plumes Their Identif. Through Time*, **352**, 359–387.
- 552 Arndt N. T., Kerr A. C. and Tarney J. (1997) Dynamic melting in plume heads: the formation of
553 Gorgona komatiites and basalts. *Earth Planet. Sci. Lett.* **146**, 289–301. Available at:
554 <http://orca.cf.ac.uk/9575/%5Cnhttp://linkinghub.elsevier.com/retrieve/pii/S0012821X9600219>
555 1.
- 556 Bédard J. H. (2018) Stagnant lids and mantle overturns: Implications for Archaean tectonics,
557 magmagenesis, crustal growth, mantle evolution, and the start of plate tectonics. *Geosci. Front.*
558 **9**, 19–49. Available at: <https://doi.org/10.1016/j.gsf.2017.01.005>.
- 559 Bennett V. C., Nutman A. P. and McCulloch M. T. (1993) Nd isotopic evidence for transient, highly
560 depleted mantle reservoirs in the early history of the Earth. *Earth Planet. Sci. Lett.* **119**, 299–
561 317.
- 562 Bouvier A., Vervoort J. D. and Patchett P. J. (2008) The Lu-Hf and Sm-Nd isotopic composition of
563 CHUR: Constraints from unequilibrated chondrites and implications for the bulk composition of
564 terrestrial planets. *Earth Planet. Sci. Lett.* **273**, 48–57.
- 565 Collins W. J. and Van Kranendonk M. J. (1999) Model for the development of kyanite during partial
566 convective overturn of Archean granite-greenstone terranes: The Pilbara Craton, Australia. *J.*
567 *Metamorph. Geol.* **17**, 145–156.
- 568 Corgne A., Liebske C., Wood B. J., Rubie D. C. and Frost D. J. (2005) Silicate perovskite-melt
569 partitioning of trace elements and geochemical signature of a deep perovskitic reservoir.
570 *Geochim. Cosmochim. Acta* **69**, 485–496.
- 571 Corgne A. and Wood B. J. (2002) CaSiO₃ and CaTiO₃ perovskite-melt partitioning of trace elements:
572 Implications for gross mantle differentiation. *Geophys. Res. Lett.* **29**, 39-1-39-4.
- 573 Davies G. F. (1992) On the emergence of plate tectonics. *Geology* **20**, 963–966.
- 574 Gardiner N. J., Hickman A. H., Kirkland C. L., Lu Y., Johnson T. and Zhao J. X. (2017) Processes of crust
575 formation in the early Earth imaged through Hf isotopes from the East Pilbara Terrane.
576 *Precambrian Res.* **297**, 56–76.
- 577 Gruau G., Jahn B. M., Glikson A. Y., Davy R., Hickman A. H. and Chauvel C. (1987) Age of the Archean
578 Talga-Talga Subgroup, Pilbara Block, Western Australia, and early evolution of the mantle: new
579 SmNd isotopic evidence. *Earth Planet. Sci. Lett.* **85**, 105–116.
- 580 Gruau G., Rosing M., Bridgwater D. and Gill R. C. O. (1996) Resetting of Sm-Nd systematics during
581 metamorphism of > 3.7-Ga rocks: Implications for isotopic models of early Earth differentiation.
582 *Chem. Geol.* **133**, 225–240.
- 583 Hickman A. H. (2012) Review of the Pilbara Craton and Fortescue Basin, Western Australia: Crustal
584 evolution providing environments for early life. *Isl. Arc* **21**, 1–31.
- 585 Hoffmann J. E., Münker C., Næraa T., Rosing M. T., Herwartz D., Garbe-Schönberg D. and Svahnberg
586 H. (2011a) Mechanisms of Archean crust formation inferred from high-precision HFSE
587 systematics in TTGs. *Geochim. Cosmochim. Acta* **75**, 4157–4178.
- 588 Hoffmann J. E., Münker C., Polat A., Rosing M. T. and Schulz T. (2011b) The origin of decoupled Hf-Nd
589 isotope compositions in Eoarchean rocks from southern West Greenland. *Geochim. Cosmochim.*
590 *Acta* **75**, 6610–6628.

591 Hoffmann J. E. and Wilson A. H. (2017) The origin of highly radiogenic Hf isotope compositions in 3.33
592 Ga Comondale komatiite lavas (South Africa). *Chem. Geol.* **455**, 6–21. Available at:
593 <http://dx.doi.org/10.1016/j.chemgeo.2016.10.010>.

594 Israel C., Boyet M., Doucelance R., Bonnand P., Frossard P., Auclair D. and Bouvier A. (2019)
595 Formation of the Ce-Nd mantle array: Crustal extraction vs. recycling by subduction. *Earth*
596 *Planet. Sci. Lett.* **1**, 1–12. Available at:
597 <https://linkinghub.elsevier.com/retrieve/pii/S0012821X19306338>.

598 Johnson T. E., Brown M., Gardiner N. J., Kirkland C. L. and Smithies R. H. (2017) Earth's first stable
599 continents did not form by subduction. *Nature* **543**, 239–242.

600 Kemp A. I., Hickman A. H. and Kirkland C. L. (2015) Report 151: Early Evolution of the Pilbara Craton
601 from Hf isotopes in detrital and inherited zircons. *Precambrian Res.* **261**, 26.

602 Klemme S., Ivanic T. J., Connolly J. A. D. and Harte B. (2009) Thermodynamic modelling of Cr-bearing
603 garnets with implications for diamond inclusions and peridotite xenoliths. *Lithos* **112**, 986–991.
604 Available at: <http://dx.doi.org/10.1016/j.lithos.2009.05.007>.

605

606 Krapez B. and Eisenlohr B. (1998) Tectonic settings of Archaean (3325–2775 Ma) crustal-supracrustal
607 belts in the West Pilbara Block. *Precambrian Res.* **88**, 173–205.

608 Lee C. T. A., Luffi P., Plank T., Dalton H. and Leeman W. P. (2009) Constraints on the depths and
609 temperatures of basaltic magma generation on Earth and other terrestrial planets using new
610 thermobarometers for mafic magmas. *Earth Planet. Sci. Lett.* **279**, 20–33.

611 Maier W. D., Barnes Stephen J., Campbell I. H., Fiorentini M. L., Peltonen P., Barnes Sarah Jane and
612 Smithies R. H. (2009) Progressive mixing of meteoritic veneer into the early Earth's deep mantle.
613 *Nature* **460**, 620–623.

614 Makishima A. and Nakamura E. (1991) Precise measurement of cerium isotope composition in rock
615 samples. *Chem. Geol.* **94**, 1–11. Available at: [http://dx.doi.org/10.1016/S0009-2541\(10\)80012-](http://dx.doi.org/10.1016/S0009-2541(10)80012-9)
616 9.

617 Marien C. S., Hoffmann J. E., Garbe-Schönberg C. D. and Münker C. (2019) Petrogenesis of
618 plagiogranites from the Troodos Ophiolite Complex, Cyprus. *Contrib. to Mineral. Petrol.* **174**, 1–
619 24. Available at: <https://doi.org/10.1007/s00410-019-1569-3>.

620 Mole D. R., Barnes S. J., Yao Z., White A. J. R., Maas R. and Kirkland C. L. (2018) The Archaean
621 Fortescue large igneous province: A result of komatiite contamination by a distinct Eo-
622 Paleoproterozoic crust. *Precambrian Res.* **310**, 365–390.

623 Münker C., Weyer S., Scherer E. and Mezger K. (2001) Separation of high field strength elements (Nb,
624 Ta, Zr, Hf) and Lu from rock samples for MC-IPMS measurements. *Geochemistry Geophys.*
625 *Geosystems* **2**, 1–19.

626 Nebel O., Arculus R. J., Ivanic T. J. and Nebel-Jacobsen Y. J. (2013) Lu-Hf isotopic memory of plume-
627 lithosphere interaction in the source of layered mafic intrusions, Windimurra Igneous Complex,
628 Yilgarn Craton, Australia. *Earth Planet. Sci. Lett.* **380**, 151–161. Available at:
629 <http://dx.doi.org/10.1016/j.epsl.2013.08.019>.

630 Nebel O., Campbell I. H., Sossi P. A. and Van Kranendonk M. J. (2014) Hafnium and iron isotopes in
631 early Archaean komatiites record a plume-driven convection cycle in the Hadean Earth. *Earth*
632 *Planet. Sci. Lett.* **397**, 111–120. Available at: <http://dx.doi.org/10.1016/j.epsl.2014.04.028>.

633 Nisbet E. G., Cheadle M. J., Arndt N. T. and Bickle M. J. (1993) Constraining the potential temperature
634 of the Archaean mantle: A review of the evidence from komatiites. *Lithos* **30**, 291–307.

635 Petersson A., Kemp A. I. S., Gray C. M. and Whitehouse M. J. (2020) Formation of early Archean
636 Granite-Greenstone Terranes from a globally chondritic mantle: Insights from igneous rocks of
637 the Pilbara Craton, Western Australia. *Chem. Geol.* **551**.

638 Petersson A., Kemp A. I. S., Hickman A. H., Whitehouse M. J., Martin L. and Gray C. M. (2019) A new
639 3.59 Ga magmatic suite and a chondritic source to the east Pilbara Craton. *Chem. Geol.* **511**, 51–
640 70. Available at: <https://doi.org/10.1016/j.chemgeo.2019.01.021>.

641 Pin C. and Zalduegui J. (1997) Sequential separation of light rare-earth elements, thorium and
642 uranium by miniaturized extraction chromatography: application to isotopic analyses of
643 silicate rocks. *Anal. Chim. Acta* **229**, 79–89.

644 Polat A., Hofmann A. W. and Rosing M. T. (2002) Boninite-like volcanic rocks in the 3.7 – 3.8 Ga Isua
645 greenstone belt, West Greenland: geochemical evidence for intra-oceanic subduction zone
646 processes in the early Earth. *Chem. Geol.* **184**, 231–254.

647 Puchtel I. S., Blichert-Toft J., Touboul M., Horan M. F. and Walker R. J. (2016) The coupled 182W-
648 142Nd record of early terrestrial mantle differentiation. *Geochemistry Geophys.*
649 *Geosystems* **17**, 1312–1338.

650 Rizo H., Boyet M., Blichert-Toft J. and Rosing M. (2011) Combined Nd and Hf isotope evidence for
651 deep-seated source of Isua lavas. *Earth Planet. Sci. Lett.* **312**, 267–279. Available at:
652 <http://dx.doi.org/10.1016/j.epsl.2011.10.014>.

653 Rizo H., Walker R. J., Carlson R. W., Touboul M., Horan M. F., Puchtel I. S., Boyet M. and Rosing M. T.
654 (2016) Early Earth differentiation investigated through 142Nd, 182W, and highly siderophile
655 element abundances in samples from Isua, Greenland. *Geochim. Cosmochim. Acta* **175**, 319–
656 336. Available at: <http://dx.doi.org/10.1016/j.gca.2015.12.007>.

657 Salters V. J. M., Mallick S., Hart S. R., Langmuir C. E. and Stracke A. (2011) Domains of depleted
658 mantle: New evidence from hafnium and neodymium isotopes. *Geochemistry, Geophys.*
659 *Geosystems* **12**, 1–18.

660 Schnabel C., Muenker C. and Strub E. (2017) La-Ce isotope measurements by Multicollector-ICPMS. *J.*
661 *Anal. At. Spectrom.* **32**, 2360–2370. Available at:
662 <http://pubs.rsc.org/en/Content/ArticleLanding/2017/JA/C7JA00256D>.

663 Smithies R. H., Champion D. C. and Van Kranendonk M. J. (2007a) Chapter 4.2 The Oldest Well-
664 Preserved Felsic Volcanic Rocks on Earth: Geochemical Clues to the Early Evolution of the
665 Pilbara Supergroup and Implications for the Growth of a Paleoarchean Protocontinent. *Dev.*
666 *Precambrian Geol.* **15**, 339–367.

667 Smithies R. H., Champion D. C. and Van Kranendonk M. J. (2009) Formation of Paleoarchean
668 continental crust through infracrustal melting of enriched basalt. *Earth Planet. Sci. Lett.* **281**,
669 298–306. Available at: <http://dx.doi.org/10.1016/j.epsl.2009.03.003>.

670 Smithies R. H., Champion D. C., Van Kranendonk M. J. and Hickman A. H. (2007b) GEOCHEMISTRY OF
671 VOLCANIC ROCKS OF THE NORTHERN PILBARA CRATON WESTERN AUSTRALIA. *GSWA Rep.* **104**,
672 48.

673 Smithies R. H., Champion D. C., Van Kranendonk M. J., Howard H. M. and Hickman A. H. (2005a)
674 Modern-style subduction processes in the Mesoarchean: Geochemical evidence from the 3.12
675 Ga Whundo intra-oceanic arc. *Earth Planet. Sci. Lett.* **231**, 221–237.

676 Smithies R. H., Champion D. C. and Sun S. S. (2004) Evidence for early LREE-enriched mantle source
677 regions: Diverse magmas from the c. 3.0 Ga Mallina Basin, Pilbara Craton, NW Australia. *J.*
678 *Petrol.* **45**, 1515–1537.

- 679 Smithies R. H., Ivanic T. J., Lowrey J. R., Morris P. A., Barnes S. J., Wyche S. and Lu Y.-J. (2018) Two
680 distinct origins for Archean greenstone belts. *Earth Planet. Sci. Lett.* **487**, 106–116. Available at:
681 <http://linkinghub.elsevier.com/retrieve/pii/S0012821X18300529>.
- 682 Smithies R. H., Van Kranendonk M. J. and Champion D. C. (2005b) It started with a plume - Early
683 Archean basaltic proto-continental crust. *Earth Planet. Sci. Lett.* **238**, 284–297.
- 684 Smithies R. H., Van Kranendonk M. J. and Champion D. C. (2007c) The Mesoarchean emergence of
685 modern-style subduction. *Gondwana Res.* **11**, 50–68.
- 686 Sossi P. A., Eggins S. M., Nesbitt R. W., Nebel O., Hergt J. M., Campbell I. H., O'Neill H. S. C.,
687 Kranendonk M. Van and Rhodri Davies D. (2016) Petrogenesis and geochemistry of Archean
688 Komatiites. *J. Petrol.* **57**, 147–184.
- 689 Tessalina S. G., Bourdon B., Van Kranendonk M., Birck J. L. and Philippot P. (2010) Influence of
690 Hadean crust evident in basalts and cherts from the Pilbara Craton. *Nat. Geosci.* **3**, 214–217.
691 Available at: <http://dx.doi.org/10.1038/ngeo772>.
- 692 Thorne A. M. and Trendall A. F. (2001) Geology of the Fortescue Group, Pilbara Craton, Western
693 Australia. *Geol. Surv. West. Aust. Bull.* **144**, 1–249.
- 694 Tusch J., Münker C., Hasenstab E., Jansen M., Marien C. S., Kurzweil F., Van Kranendonk M. J.,
695 Smithies R. H., Maier W. D. and Garbe-Schönberg D. (in review) Convective isolation of Hadean
696 mantle reservoirs through Archean time. *PNAS*
- 697 Van Kranendonk M. J. (2010) Two types of Archean continental crust: Plume and plate tectonics on
698 early earth. *Am. J. Sci.* **310**, 1187–1209.
- 699 Van Kranendonk M. J., Collins W. J., Hickman A. and Pawley M. J. (2004) Critical tests of vertical vs.
700 horizontal tectonic models for the Archean East Pilbara Granite-Greenstone Terrane, Pilbara
701 Craton, Western Australia. *Precambrian Res.* **131**, 173–211.
- 702 Van Kranendonk M. J., Hickman A. H., Smithies R. H. and Nelson D. R. (2002) Geology and tectonic
703 evolution of the Archean North Pilbara Terrain, Pilbara Craton, Western Australia. *Econ. Geol.*
704 **97**, 695–732.
- 705 Van Kranendonk M. J., Hugh Smithies R., Hickman A. H. and Champion D. C. (2007) Review: Secular
706 tectonic evolution of Archean continental crust: interplay between horizontal and vertical
707 processes in the formation of the Pilbara Craton, Australia. *Terra Nov.* **19**, 1–38.
- 708 Van Kranendonk M. J., Hugh Smithies R., Hickman A. H., Wingate M. T. D. D. and Bodorkos S. (2010)
709 Evidence for Mesoarchean (~3.2 Ga) rifting of the Pilbara Craton: The missing link in an early
710 Precambrian Wilson cycle. *Precambrian Res.* **177**, 145–161.
- 711 Van Kranendonk M. J., Smithies R. H., Griffin W. L., Huston D. L., Hickman A. H., Champion D. C.,
712 Anhaeusser C. R. and Pirajno F. (2015) Making it thick: a volcanic plateau origin of
713 Palaeoarchean continental lithosphere of the Pilbara and Kaapvaal cratons. *Geol. Soc. London,
714 Spec. Publ.* **389**, 83–111.
- 715 Vervoort J. D. and Blichert-Toft J. (1999) Evolution of the depleted mantle: Hf isotope evidence from
716 juvenile rocks through time. *Geochim. Cosmochim. Acta* **63**, 533–556.
- 717 Vervoort J. D., Patchett P. J., Albarède F., Blichert-Toft J., Rudnick R. and Downes H. (2000) Hf-Nd
718 isotopic evolution of the lower crust. *Earth Planet. Sci. Lett.* **181**, 115–129.
- 719 Wiemer D., Schrank C. E., Murphy D. T., Wenham L. and Allen C. M. (2018) Earth's oldest stable crust
720 in the Pilbara Craton formed by cyclic gravitational overturns. *Nat. Geosci.* **11**, 357–361.
- 721 Willbold M. (2007) Determination of Ce isotopes by TIMS and MC-ICPMS and initiation of a new,

722 homogeneous Ce isotopic reference material. *J. Anal. At. Spectrom.* **22**, 1364–1372.

723 Willig M. and Stracke A. (2019) Earth's chondritic light rare earth element composition: Evidence
724 from the Ce–Nd isotope systematics of chondrites and oceanic basalts. *Earth Planet. Sci. Lett.*
725 **509**, 55–65. Available at: <https://doi.org/10.1016/j.epsl.2018.12.004>.

726

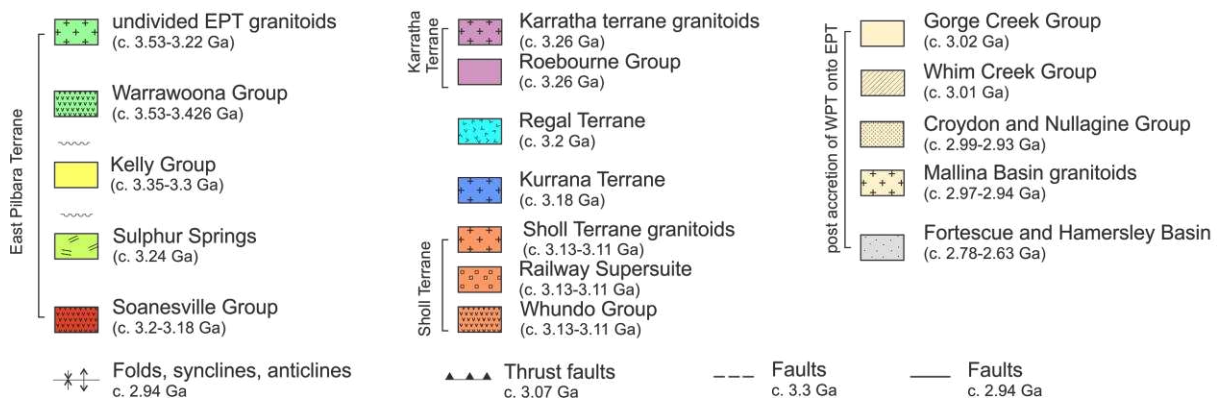
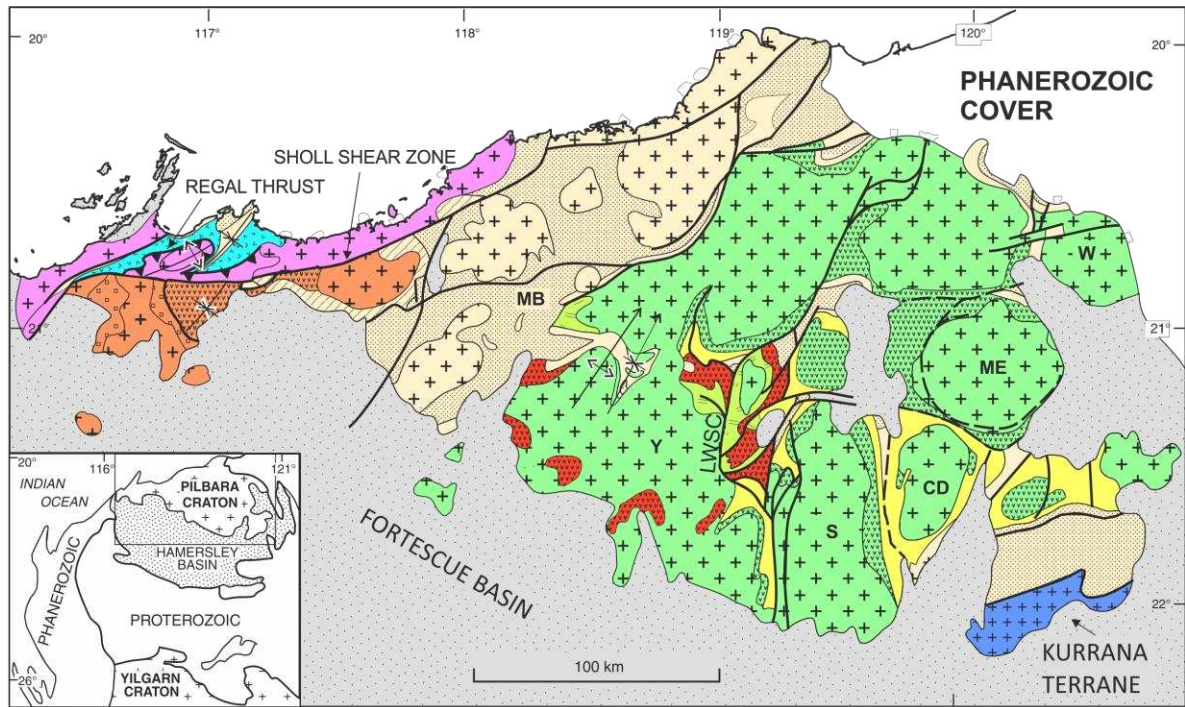


Fig. 1: Simplified geological map of the northern Pilbara Craton, showing greenstones and granitoids of the East Pilbara Terrane, Kurrana Terrane, Karratha Terrane, Regal Terrane, Sholl Terrane and the late volcano-sedimentary Mallina Basin and De Grey Supergroup (MB=Mallina Basin; MCB=Mosquito Creek basin) and Fortescue Basin. Abbreviations for different granitoids that were sampled in this study: CD=Corunna Downs; ME=Mount Edgar; S=Shaw; W=Warrawagine; Y=Yule. Modified after Van Kranendonk et al., (2007a), (2010).

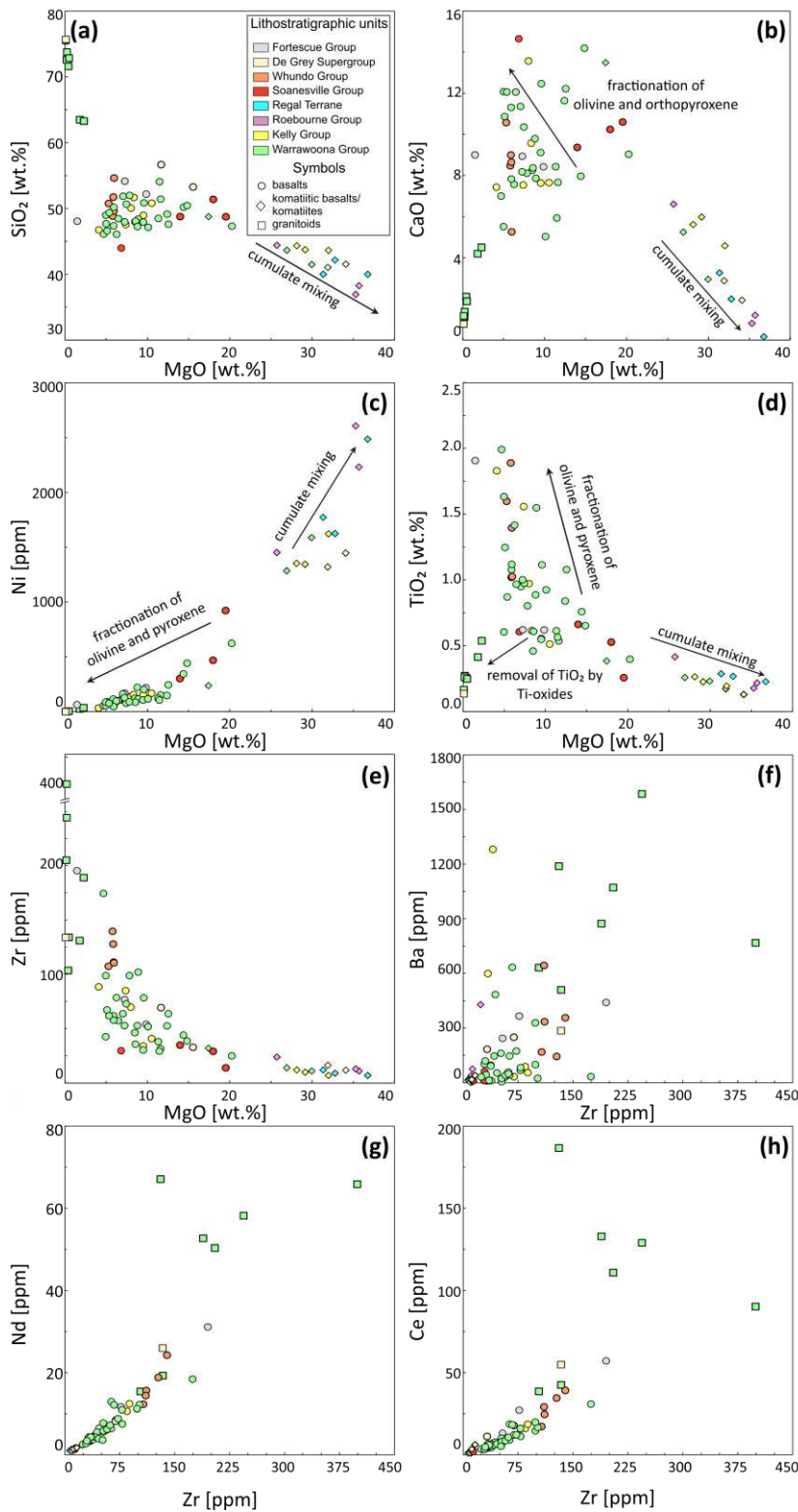


Fig. 2: Co-variation diagrams for selected major and trace elements in mafic-ultramafic to felsic Pilbara Craton samples a) - e) Selected major and trace elements plotted against MgO demonstrate the preservation of pristine igneous fractionation trends. f) Barium vs. Zr plot illustrating post-magmatic disturbances of large ion lithophile elements. g) and h) show preserved igneous trends for Ce, Nd and Hf (not shown) with Zr, implying that the elements relevant for radiogenic isotope measurements have preserved their pristine igneous composition. Shown symbols also include data from Maier et al., (2009) and Tusch et al., (2020) for samples that were also analyzed in this study.

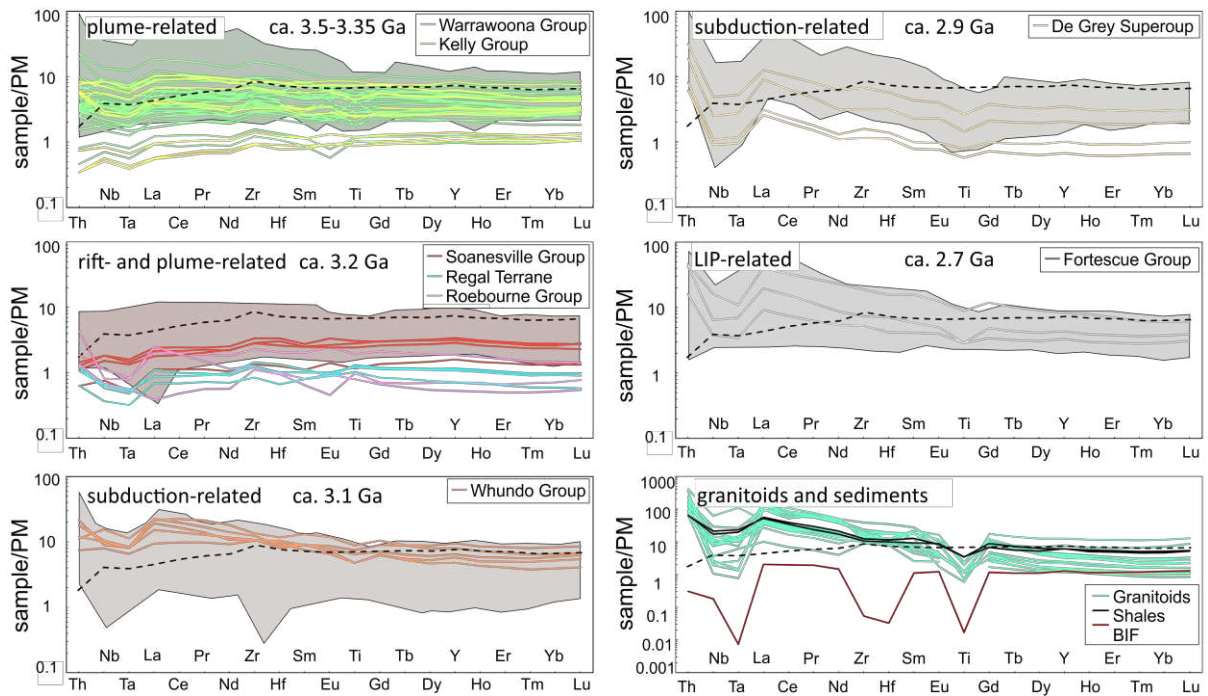


Fig. 3: Primitive mantle (PM) normalized incompatible trace element patterns for selected stratigraphic units, rock types, and geological settings. Additional data from Tusch et al., (2020) for samples that were also analyzed in this study. Colored fields represent compiled literature data. Detailed references for mantle reservoirs shown here are given in supplementary file S0.

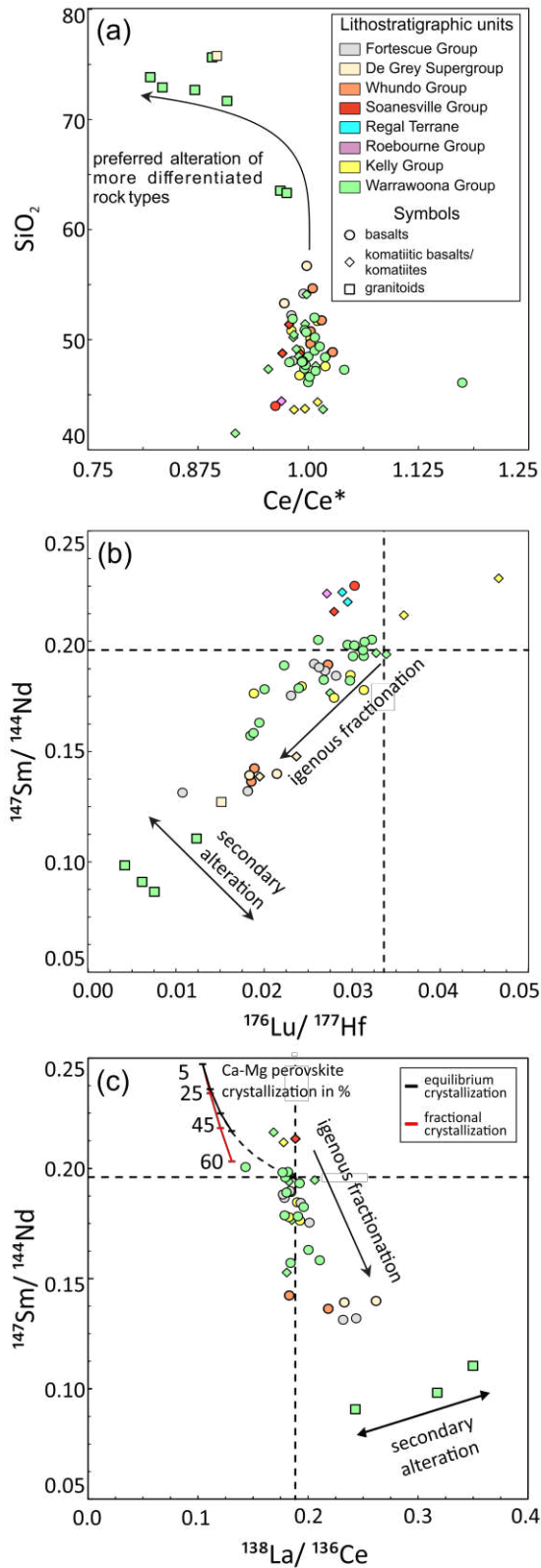


Fig. 4: Plots illustrating alteration features in Pilbara rocks. a) Ce/Ce^* anomalies increase with increasing SiO_2 . b) and c) co-variations of parent/daughter ratios of relevant radiogenic isotope systems indicate, that the majority of samples have preserved their pristine magmatic geochemistry. Additional data from Tusch et al., (2020) for samples that were also analyzed in this study.

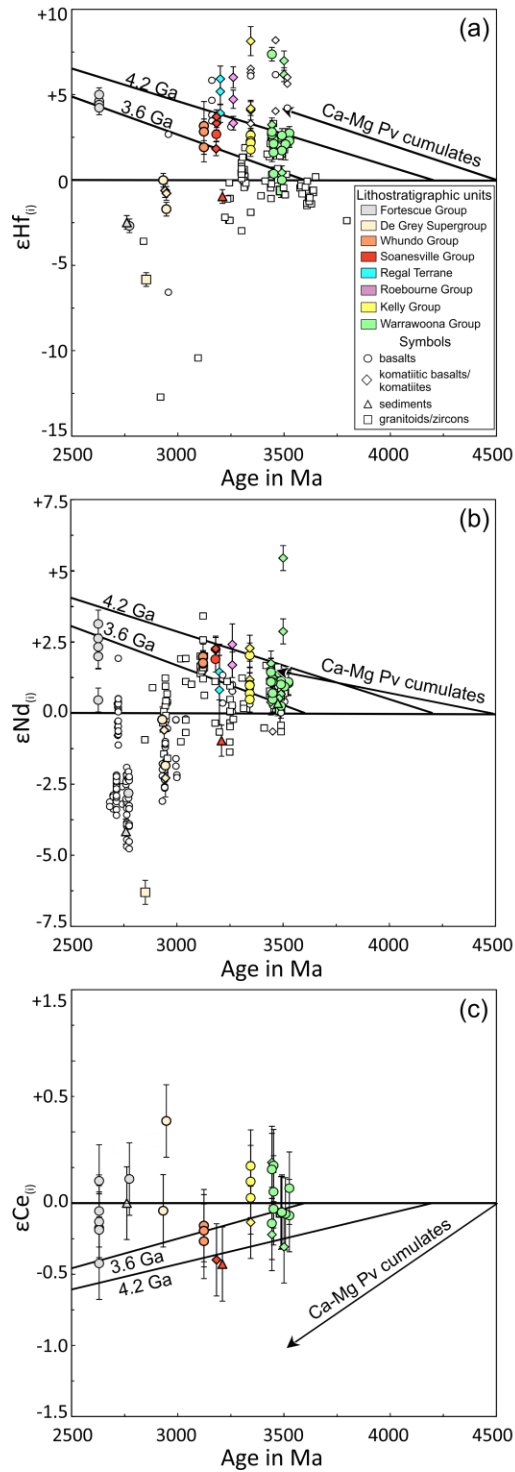


Fig. 5: Evolution of radiogenic isotope compositions in Pilbara rocks through geologic time. Panels illustrate a) initial Hf, b) initial Nd, and c) initial Ce isotope compositions. For Hf and Nd isotope compositions, our samples show a constant increase between ca. 3.59-3.18 Ga for most samples with the marked exception of the majority of 3.34 Ga Kelly Group samples. After 3.12 Ga, the Pilbara Craton develops towards more radiogenic Ce and less radiogenic Nd and Hf isotope compositions, reflecting a subduction-like setting and/or crustal contamination of older felsic crust. Additional literature data from the Pilbara Craton are shown here with smaller symbol sizes and without colors. Detailed references for literature data shown here are given in supplementary file S0. Errors are only shown for samples of this study and include the propagated errors of the external reproducibility on isotope composition measurements, measured parent/daughter ratios and the errors of the crystallization age of each specific formation. If the individually measured 2 S.E. was larger than the external reproducibility, we chose this error for the error propagation.

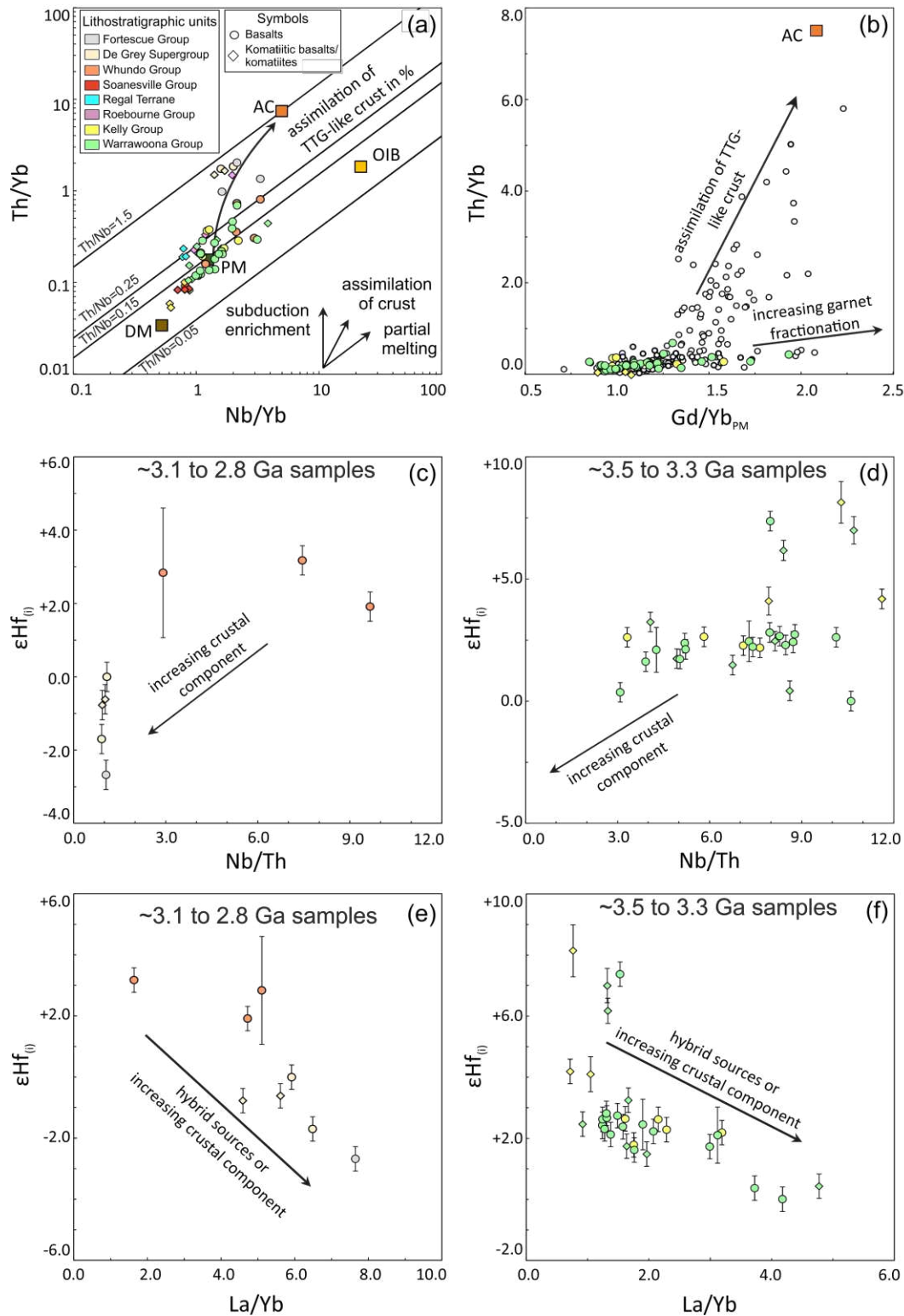


Fig. 6: Isotope and trace element variations illustrating effects of crustal contamination for selected suites. a) All ≤ 2.9 Ga samples b) but only some Paleoproterozoic samples have inherited an enriched component with high Th/Yb. c) and d) Hybrid mantle sources are likely responsible for decreased $\epsilon\text{Hf}(t)$ values of some EPT samples and not continental crust, as no co-variations between $\epsilon\text{Hf}(t)$ or $\epsilon\text{Nd}(t)$ with Nb/Th are observed, e) and f) but with La/Yb. Co-variations of $\epsilon\text{Hf}(t)$ with La/Yb and Th/Nb in younger successions, however, indicate mixing with crustal components rather than hybrid mantle sources. Additional literature data are taken from Tusch et al., (2020) for samples of this study. Additional literature data from the Pilbara Craton are shown here with smaller symbol sizes and without colors. Detailed references for literature data and various mantle reservoirs shown here (DM=depleted mantle, PM=primitive mantle, OIB=ocean island basalt, AC=Archean TTG-like crust), are given in supplementary file S0. Error estimates are the same as in Figure 5.

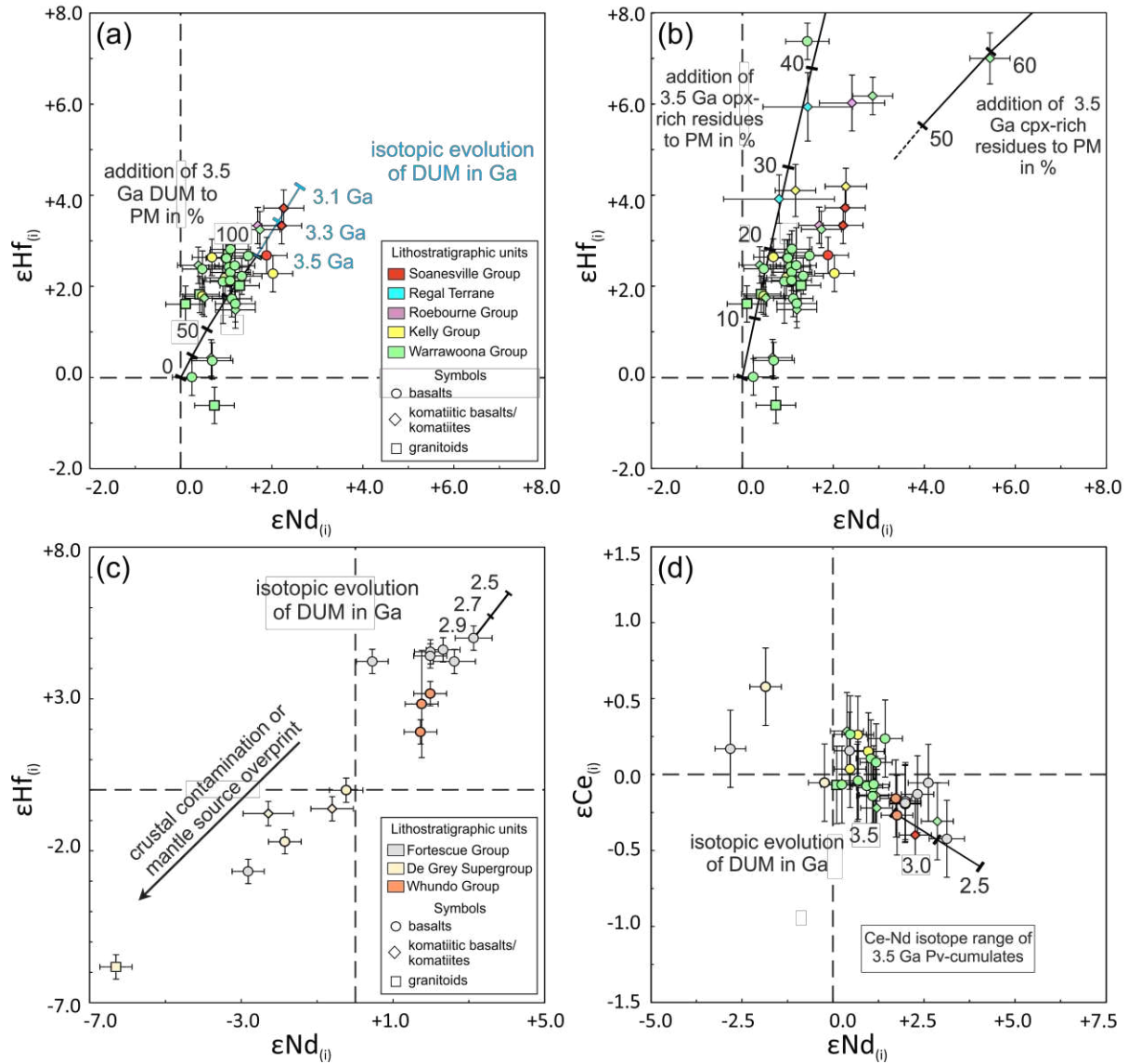


Fig. 7: Co-variation diagrams between initial Ce, Nd and Hf isotope compositions. a) $\epsilon\text{Hf}_{(i)}$ vs. $\epsilon\text{Nd}_{(i)}$ for 3.53-3.12 Ga samples show an increase of initial $\epsilon\text{Hf}_{(i)}$ and $\epsilon\text{Nd}_{(i)}$ values for most mafic samples with time that is best explained by an evolving depleted upper mantle (DUM) component. b) Some samples, in particular komatiites, are decoupled in their $\epsilon\text{Hf}_{(i)}$ and $\epsilon\text{Nd}_{(i)}$ composition, which is best explained by mixing of primitive mantle with older (~4.2 Ga) residual mantle domains showing decoupled Hf-Nd isotope compositions due to residual garnet. c) Refertilization of the mantle source or crustal contamination can explain the decreased $\epsilon\text{Hf}_{(i)}$ vs. $\epsilon\text{Nd}_{(i)}$ values found in some 2.94-2.63 Ga samples. d) Values of $\epsilon\text{Ce}_{(i)}$ vs $\epsilon\text{Nd}_{(i)}$ of unaltered samples show a coherent evolution compared to the $\epsilon\text{Hf}_{(i)}$ and $\epsilon\text{Nd}_{(i)}$ trend. Importantly, the Hf-Nd-Ce arrays defined by the Pilbara samples all overlap the chondritic value, with an Hf-Nd array for coupled samples of $\epsilon\text{Hf}_{(i)} = 1.2 (\pm 0.2) \times \epsilon\text{Nd}_{(i)} + 0.53 (\pm 0.6)$ that is indistinguishable from the modern day Hf-Nd mantle array. The Ce-Nd array is defined by: $\epsilon\text{Ce}_{(i)} = -0.14 (\pm 0.07) \times \epsilon\text{Nd}_{(i)} - 0.08 (\pm 0.3)$ and also overlaps with the present day Ce-Nd array (Israel et al., 2019). Error estimates are the same as in Figure 5.

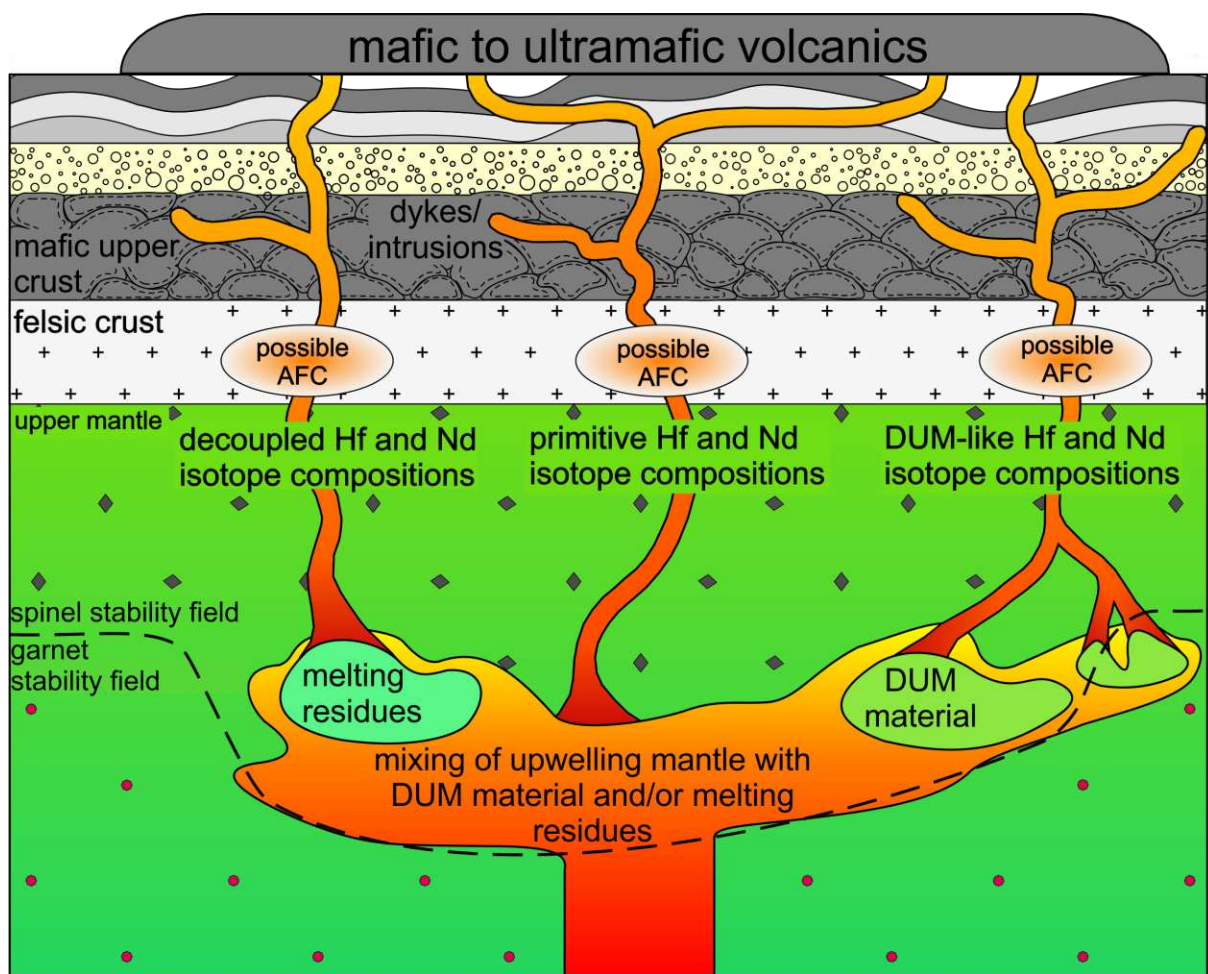


Fig 8: Sketch illustrating our proposed geodynamic model for the early evolution of the Pilbara craton as preserved in the EPT. Between ca. 3.5 to 3.3 Ga, near-primitive upwelling mantle mixes with ca. 4.2 Ga old depleted upper mantle (DUM) material and in some cases with residual mantle domains depleted in the garnet stability field. With such hybrid mantle sources (near primitive and garnet-bearing residual mantle domains), the pooled melts may have decoupled Hf-Nd isotope compositions. In contrast, mixing of near-primitive and DUM material (which is most frequent) generates melts that are not decoupled in their Hf and Nd isotope composition and lie in $\epsilon\text{Hf}_{(t)}$ vs. $\epsilon\text{Nd}_{(t)}$ space somewhere between primitive mantle and DUM recalculated to the time of eruption. Furthermore, the eruption of near-primitive mantle melts that have not mixed with residual domains or DUM material also occurred, although this compositional type must have been rare as only few samples are characterized by near-chondritic Hf and Nd isotope compositions.